



## Active tectonics of the Northern Rif (Morocco) from geomorphic and geochronological data

A Poujol, J-F Ritz, A Tahayt, P Vernant, M Condomines, P-H Blard, J Billant, L Vacher, B Tibari, L Hni, et al.

### ► To cite this version:

A Poujol, J-F Ritz, A Tahayt, P Vernant, M Condomines, et al.. Active tectonics of the Northern Rif (Morocco) from geomorphic and geochronological data. *Journal of Geodynamics*, 2014, 77, pp.70 - 88. 10.1016/j.jog.2014.01.004 . hal-04744130

HAL Id: hal-04744130

<https://hal.science/hal-04744130v1>

Submitted on 18 Oct 2024

**HAL** is a multi-disciplinary open access archive for the deposit and dissemination of scientific research documents, whether they are published or not. The documents may come from teaching and research institutions in France or abroad, or from public or private research centers.

L'archive ouverte pluridisciplinaire **HAL**, est destinée au dépôt et à la diffusion de documents scientifiques de niveau recherche, publiés ou non, émanant des établissements d'enseignement et de recherche français ou étrangers, des laboratoires publics ou privés.



Contents lists available at ScienceDirect

# Journal of Geodynamics

journal homepage: <http://www.elsevier.com/locate/jog>



## Active tectonics of the Northern Rif (Morocco) from geomorphic and geochronological data

A. Poujol<sup>a,\*</sup>, J.-F. Ritz<sup>a</sup>, A. Tahayt<sup>b</sup>, P. Vernant<sup>a</sup>, M. Condomines<sup>a</sup>, P.-H. Blard<sup>c</sup>, J. Billant<sup>d</sup>, L. Vacher<sup>a</sup>, B. Tibari<sup>c</sup>, L. Hni<sup>b</sup>, A. Koulali Idrissi<sup>e</sup>

<sup>a</sup> Geosciences Montpellier, CNRS-University of Montpellier, Montpellier, France

<sup>b</sup> CNRST, Institut National de Géophysique, Rabat, Morocco

<sup>c</sup> CRPG, UPR 2300, CNRS, Nancy-Université, Vandoeuvre-lès-Nancy, France

<sup>d</sup> CEREGE – UMR CNRS, University of Aix-Marseille, Aix-en-Provence, France

<sup>e</sup> Research School of Earth Sciences, The Australian National University, Canberra, ACT, Australia

### ARTICLE INFO

#### Article history:

Received 17 May 2013

Received in revised form 15 January 2014

Accepted 27 January 2014

Available online xxx

#### Keywords:

Active tectonics

<sup>3</sup>He cosmogenic

Morocco

Al-Hoceima

Geomorphology

### ABSTRACT

We present results of a geomorphological and morphotectonic analysis of the northeastern part of the Rif. We show that the present day kinematics of the Rif is characterized by active deformation along the Trougout and Nekor faults in the North-East. Digital Elevation Models of offset drainage features (streams, fluvial terraces) allow determining a normal-left-lateral motion along the Trougout fault and a left-lateral strike-slip motion along the Nekor fault. Preliminary <sup>3</sup>He cosmogenic dates of tectonic markers yield vertical and horizontal slip rates of ~0.9 mm/yr and ~0.5 mm/yr, respectively along the Trougout fault. The present-day localized transtension seen in the north-eastern Rif morphology (Ras Tarf) is coeval with uplifted marine terraces near the Al Hoceima Bay. U/Th dating of shells yield an average uplift rate of ~0.2 mm/yr during the past 500 ka. These data show that active transtension in the northeastern Rif is also associated with uplift. These new morphotectonic constraints are consistent with the GPS measurements showing southwestward overall motion of most of the Rif belt with respect to stable Africa.

© 2014 Elsevier Ltd. All rights reserved.

## 1. Introduction

The Moroccan Rif Cordillera is located at the southern part of the Gibraltar arc and constitutes together with the Betic mountain belt, the westernmost termination of the peri-Mediterranean Alpine mountain range. It results from the convergence between the African and the Eurasian plates since the Upper Cretaceous. This convergence is still active as shown by a regular seismic activity and several destructive historical earthquakes. Geodetic studies show that the general convergence rate between Africa and Eurasia is  $4.3 \pm 0.5$  mm/yr with an azimuth of  $116 \pm 6^\circ$  (McClusky et al., 2003). This present-day deformation pattern is consistent with tectonic studies that show Mio-Pliocene NW-SE compression (Meghraoui et al., 1996; Moratti et al., 2003; Tahayt et al., 2009). However, GPS studies show that the Rif is moving perpendicularly to the general WNW-ESE Africa-Eurasia convergence direction (Fadil et al., 2006; Vernant et al., 2010) (Fig. 1A).

Despite the GPS velocity field and a few pioneering tectonic studies (Ait Brahim and Chotin, 1990; Meghraoui et al., 1996; Moratti et al., 2003; Rampnoux et al., 1977), the distribution and

kinematics of the present-day deformations in the Rif remains poorly constrained.

In this paper, we bring new insights on the active deformations affecting the northeastern Rif, using satellite imagery, 1:30,000 scale aerial photographs, Digital Elevation Models (DEMs) at different scales and field surveys. Our study allows characterizing the present-day active faulting in terms of location, kinematics and uplift rates in the northeastern Rif.

## 2. Tectonic setting

The tectonic evolution of the Rif mountain range reflects overprinted deformations dominated by the ongoing Eurasian-African plate convergence since the Upper Cretaceous (Lonergan and White, 1997). This deformation started with the subduction of the Neotethys Ocean (Faccenna et al., 2004) and is closely related to the extension giving way to the Alboran Sea since the Middle Miocene (Lonergan and White, 1997).

The structural units of the Rif mountains are classically grouped into three domains: the Internal and External Zones, separated by the Maghrebian Flysch units (Waldi, 1983) (Fig. 1A). The Internal Zone is mainly composed of Triassic to Miocene sedimentary rocks metamorphosed at high-pressure/low-temperature conditions during the Eocene-Late Oligocene main Alpine deformation

\* Corresponding author. Tel.: +33 467143894.

E-mail address: [antoine.poujol@univ-montp2.fr](mailto:antoine.poujol@univ-montp2.fr) (A. Poujol).

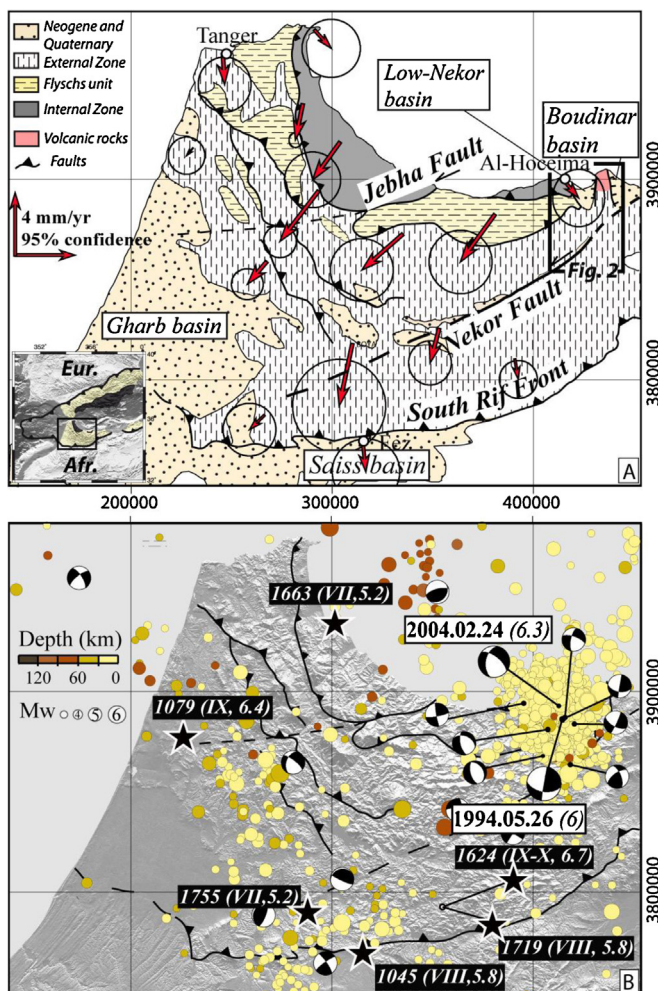


**Fig. 1.** (A) Structural and geological map of the Rif Cordillera, simplified from Chalouan et al. (2006). Red arrows are GPS site velocities with respect to Africa and 95% confidence ellipses (after Vernant et al., 2010). (B) Seismotectonic map with major faults drawn on SPOT5 DEM. The instrumental seismicity is from IRIS catalog (<http://wwwiris.edu/SeismiQuery/sq-events.htm>). Focal mechanisms are from RCMT catalog (<http://wwwboingv.it/RCMT/searchRCMT.html>) and Meghraoui et al. (1996). Note that the focal mechanisms of 1994 and 2004 events were underlined. Black and white stars indicate location of the epicenters of historical earthquakes with the date, MSK intensity and estimated magnitude after the distribution and amount of damages (after Pelaez et al., 2007). (For interpretation of the references to color in this figure legend, the reader is referred to the web version of the article.)

(Kornprobst, 1974; Chalouan and Michard, 2004). The structures mainly consist in folds and thrusts with a west to south-west vergence. Thus, the Internal Zone was thrust onto the Maghrebian Flyschs. The External Zone is composed of pelitic and carbonate Mesozoic and Cenozoic rocks deposited on the North African passive continental paleomargin. It underwent the alpine deformation mostly during the Late Tortonian that led to an arcuate south-verging general structure. The southwestern overthrusting was controlled by two main NE-SW faults (Jebha and Nekor) that played the role of lateral ramps. The Nekor fault appears as a major NE-SW linear structure that may reach an overall length of more than 200 km (Fig. 1A) (Chalouan et al., 2006). However, it is not clear whether the southern part of the Nekor fault bends westwards, or extends down to the Southern Rif front. At its northeastern end, the Nekor fault bounds the east side of the Messinian to Quaternary basin of Boudinar and is sealed by sediments of Late-Tortonian-Messinian age (Choubert et al., 1984).

The southern boundary of the Rif mountain range corresponds to the E-W trending south-verging Rif thrust (Chalouan et al., 2001; Leblanc and Olivier, 1984; Maldonado and Comas, 1992).

In several parts of the Rif range, Neogene-Quaternary sedimentary basins developed over the previous described units. They correspond to Plio-Quaternary foreland basins to the southwest (Gharb and Saïss basins) and Messinian-Quaternary basins to the northeast (low-Nekor and Boudinar basins). These basins are deformed attesting of a post-Messinian tectonic activity. Volcanic rocks of Tortonian-Messinian age form the Ras Tarf cape (El Azzouzi et al., 1999; El Bakkali et al., 1998) between the low-Nekor and the Boudinar basins.

From the compilation of kinematic analyses of Plio-Quaternary fault populations, Meghraoui et al. (1996) proposed a N-S to NW-SE main compressional stress direction with a maximum shortening rate of 1–2.3 mm/yr within the Rif. Along the Nekor fault, according to paleo-topography studies and field works (Ait Brahim et al., 1990; Morel, 1987), Meghraoui et al. (1996) estimated a shortening rate of ~2.3 mm/yr since the Pliocene which would suggest that all the shortening is resolved along the Nekor fault. In Al-Hoceima, these authors noticed a system of NS graben structure bordered by Quaternary normal faults (Ajdir, Imzourene and Trougout). On the other hand, Galindo-Zaldívar et al. (2009) consider the Nekor fault as inactive, while the Trougout and Boudinar faults bounding the Ras Tarf massif would correspond to active normal faults. From detailed fieldwork and gravimetric measurements, these authors point out an asymmetric filling of 400 m of Plio-Quaternary sediments of the low-Nekor basin with an eastward tilt of the basement along the Trougout fault and the occurrence of a blind normal fault along the western border of the basin in addition to the eastern bounding Ajdir-Imzourene faults.

The region of Al-Hoceima is also described as an uplifting region from the study of marine terraces. After the geological map (Choubert et al., 1984), three Quaternary marine terraces were mapped: the first one located at 10 m above the sea level (a.s.l.), is attributed to the MIS 5e (130 ka), the second, located between 30 and 70 m a.s.l., is attributed to the MIS 11–13 (427–528 ka), and the last one situated at 150 m a.s.l. would be attributed to the MIS 15 (621 ka). Detailed studies about the Mediterranean marine terraces from the upper Pleistocene to Holocene (Morel, 1987; Meghraoui, 1991; Meghraoui et al., 1996; Rampnoux et al., 1977) show that the Rif Mediterranean shoreline is uplifting at a rate of 0.2 mm/yr.

In the southern Rif, the structural study of Moratti et al. (2003) and Bargach et al. (2004) indicate that the E-W-trending frontal thrust of the Rif is still active with a shortening direction oriented N-S to NW-SE.

At the present-day, the Rif is still deforming with a moderate instrumental seismicity (Fig. 1B) distributed over a several hundred kilometers wide zone (Calvert et al., 2000; Buforn et al., 1991). The seismic events recorded in the region between 1970 and 2013 are clustered along a NNE-SSW-oriented zone in the Al-Hoceima and Nekor fault areas, a NE-SW-oriented zone in the southern Rif front, and a likely NNW-SSE-oriented zone in the western Rif.

The largest earthquakes took place in the Al-Hoceima region on 05/26/1994 (Mw 6) and 02/24/2004 (Mw 6.3) (Calvert et al., 1997; Stich et al., 2005; Tahayt et al., 2009). The latter event corresponds to the highest magnitude ever instrumentally recorded in the westernmost Mediterranean. The focal mechanisms of the region calculated for the period 1968–2004 attest of normal and left-lateral strike-slip faulting trending roughly N-S (El Alami et al., 1998; Stich et al., 2005; Medina and El Alami, 2006) (Fig. 1B).

In the southern Rif, in the Fez-Meknes area, the historical seismicity indicates that at least five Mw > 5.5 earthquakes were

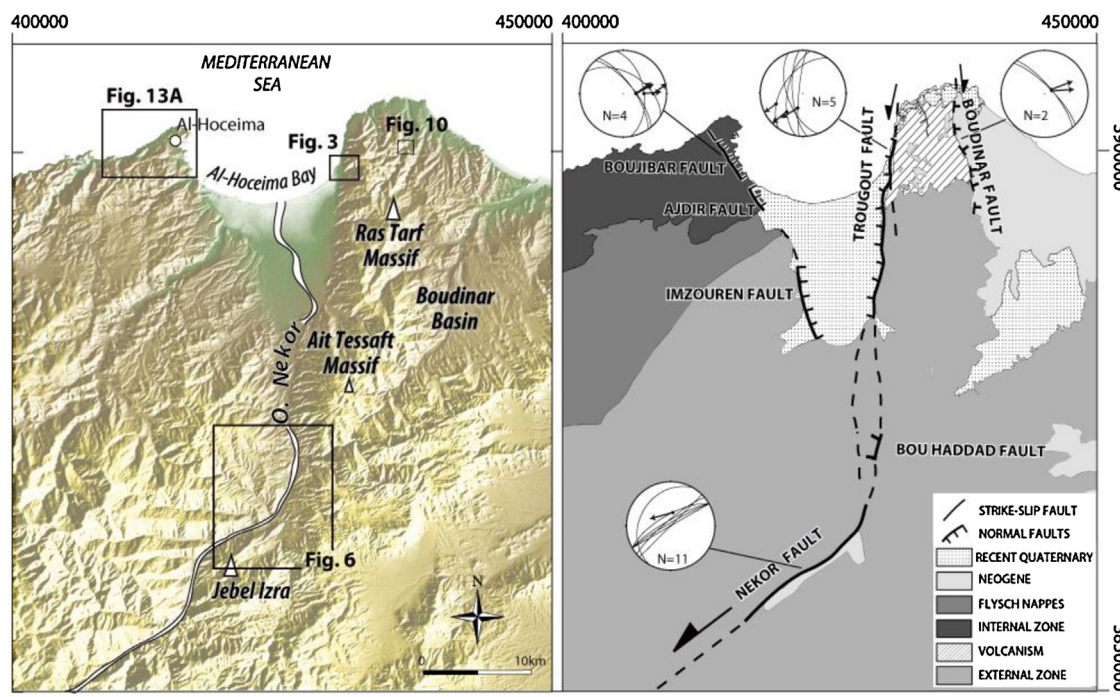


**Fig. 2.** SPOT5 DEM (left) and geological map (right) of Al-Hoceima region including active structures and stereographic plots of fault planes and striae. Black squares indicate location of studies areas. Black lines with ticks: normal fault; black lines with arrows: strike-slip faults; white triangles: mountain.

recorded since 1045AD. After Moratti et al. (2003), the latest damaging historical earthquake in the region occurred in November 27, 1755, and was located between Fez and Meknes (Fig. 1B).

Based on GPS data, Vernant et al. (2010) proposed a block model in which the present motion of the Rif range is controlled by strike-slip displacements along its eastern and western borders, while its southern front is characterized by a left-lateral transpressive deformation. The block model gives a left-lateral slip rate of  $2.6 \pm 0.8$  mm/yr along the NNE-SSW eastern border, a right-lateral slip rate of  $2.9 \pm 0.7$  mm/yr along the NNE-SSW western border,

and a shortening rate of  $2.9 \pm 0.7$  mm/yr within the EW trending southern front of the Rif.

### 3. Morphotectonic analysis

We have carried out a detailed morphotectonic analysis within the northeastern part of the Rif (Fig. 1A). To do so we have mapped geomorphic markers and quantify their deformation using satellite imagery, 1:30,000 scale aerial photographs, DEMs at different scales and field surveys.

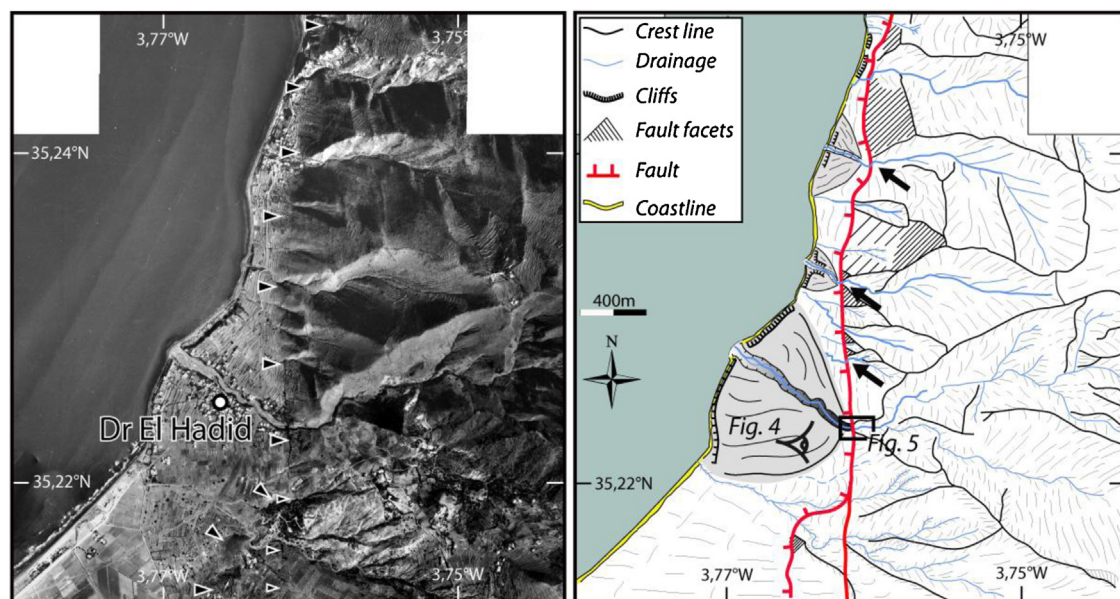


**Fig. 3.** Aerial photograph (left, September 29, 2003, 1:30,000 scale) of the Trougout fault on the western side of Rastarf massif and associated geomorphologic interpretation (right). Black triangles point out the segments of the fault (left); black arrows show the left-lateral shifted rivers (right). Gray colors correspond to the main alluvial fan surfaces. Hatched black lines show the fault facets and indicate the slip direction of the fault.

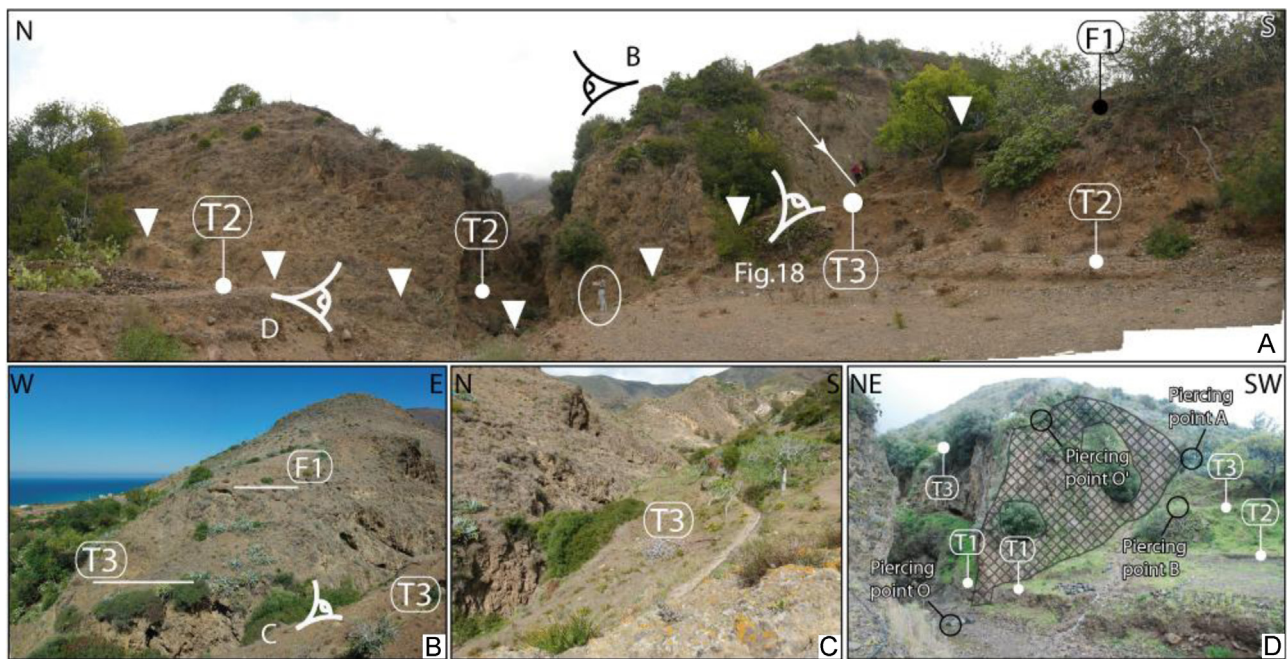


**Fig. 4.** Field views of the Trougout fault scarp affecting the quaternary alluvial terraces. The tips of the white triangles point out the base of the scarp (A). White filled dots (A and D) point out the top of the riser of the alluvial terraces, numbered from younger to older (T1, T2, T3 and F1). Black circles points out the markers (piercing points) used to estimate cumulative horizontal and vertical displacements along the fault (D); white arrow indicates the slip direction of the fault (A); hatched black lines show the fault plan (D); the circled person gives the scale of the picture (A).

### 3.1. The bay of Al-Hoceima and the Ras Tarf massif

#### 3.1.1. The Trougout Fault

The Trougout fault corresponds to the main fault separating the Bay of Al-Hoceima to the West from the Ras Tarf volcanic massif to the East (Fig. 2). The photo-interpretation of 1:30,000 scale aerial pictures (taken in September 29, 2003) allows mapping the fault and showing that it is divided in several NS trending segments that step right-laterally (Fig. 3). In the northernmost sector, the fault consists of a 7 km-long segment connecting to the south another ~26 km long segment via a bended zone forming an 800 m wide right-stepping jog (Fig. 3). The fault marks the contact between andesitic breccia of the Tortonian-Messinian Ras Tarf formation or Flysch nappes and the Quaternary Nekor deposits (Fig. 2B). The alignment of triangular facets and the occurrence of left-lateral shifted streams at the outlets of the catchments incising the Ras Tarf massif suggest a vertical and left-lateral deformation along the fault (Fig. 3).

Near Dr El Hadid village ( $N35.224047^\circ$ ,  $W3.761298^\circ$ , Elevation 50 m), the fault zone is sub-vertical and consists of a ~1–2 m thick sheared volcanic breccia (Fig. 4A). The western face of the brecciated zone displays an outstanding slickenside on which striae are well preserved (Fig. 4A). Field observations and fault slip data measured along the plane ( $N5^\circ E/82^\circ W$ , pitch of  $60^\circ S$ ) indicate a clear transtensional movement (Fig. 2B). At this site, the normal-left-lateral Trougout fault cuts the El-Hadid river which forms a 20 m deep canyon in the Ras Tarf volcanic formation within the footwall block, and continuing within the hanging wall block as a 15 m-deep gully incising a thick alluvial fan (F1). Within the hanging wall, several fill-in terraces are entrenched into the fan deposits (T1 to T3, from the youngest to the oldest, respectively) (Figs. 4A, C and 5B). T1, T2, T3 terraces are observed within the left riverbank while T2 is only observed on the right one. We interpret this asymmetric pattern as the result of the left-lateral strike-slip component of the displacement along the fault that allows

preserving the left bank of the river while the right bank, gradually moving in front of the canyon, is eroded by the river. The occurrence of T2 on both banks in the hangingwall shows that not much movement occurred since its aggradation inset in previous alluvial markers.

Within the footwall, remnants of the apex of fan surface F1 and of T3 terrace can be observed within the right bank (Fig. 4B). On the left bank, the strath surface associated with T3 terrace is well marked although the surface itself and its associated deposits have been disturbed by human activity (Fig. 4C). T2 and T1 terraces are found inside the canyon (Fig. 4A and D).

T1, T2 and T3 terraces contain decimeter-sized clasts, mostly basaltic and andesitic floating in a sandy-silty matrix, while F1 fan surface is made up of meter-to-decimeter-scale basaltic (~70%) and quartzite (~30%) boulders also included in a sandy-silty matrix.

Fig. 5 shows a DEM interpolated from RTK-GPS and total station surveys, which allows estimating the displacements of the terraces along the fault. From profiles crossing the different surfaces we have measured the minimum vertical slip for F1 and T3. Profile No. 1 yields a minimum offset of 20.7 m for F1, and profiles Nos. 2, 3 and 4 yield a minimum offset of 10.2 m for T3 (Fig. 5C). T2 and T1 are found at the same elevation at both sides of the fault, thus suggesting that they have not been displaced yet (see Fig. 4A and C and profile No. 5, in Fig. 5C).

To estimate the horizontal displacements of morphological markers along the fault plane, we use the distance between two markers (so called piercing points), corresponding to the intersection of two morphological objects with the fault. In our case, we compare the intersection with the fault, of the upper edge of F1-T3 (A) and T3-T2 (B) left bank risers respectively and of the canyon axis when depositing (O for the actual stream axis and O' for the left bank upper edge of the canyon) (Fig. 4D). Thus, using these four piercing points, we estimate cumulative horizontal displacements comprised between 25 m (O'A) and 35 m (OA) for F1-T3 riser, and between 6 m (O'B) and 16 m (OB) for T3-T2 riser (Fig. 5A).

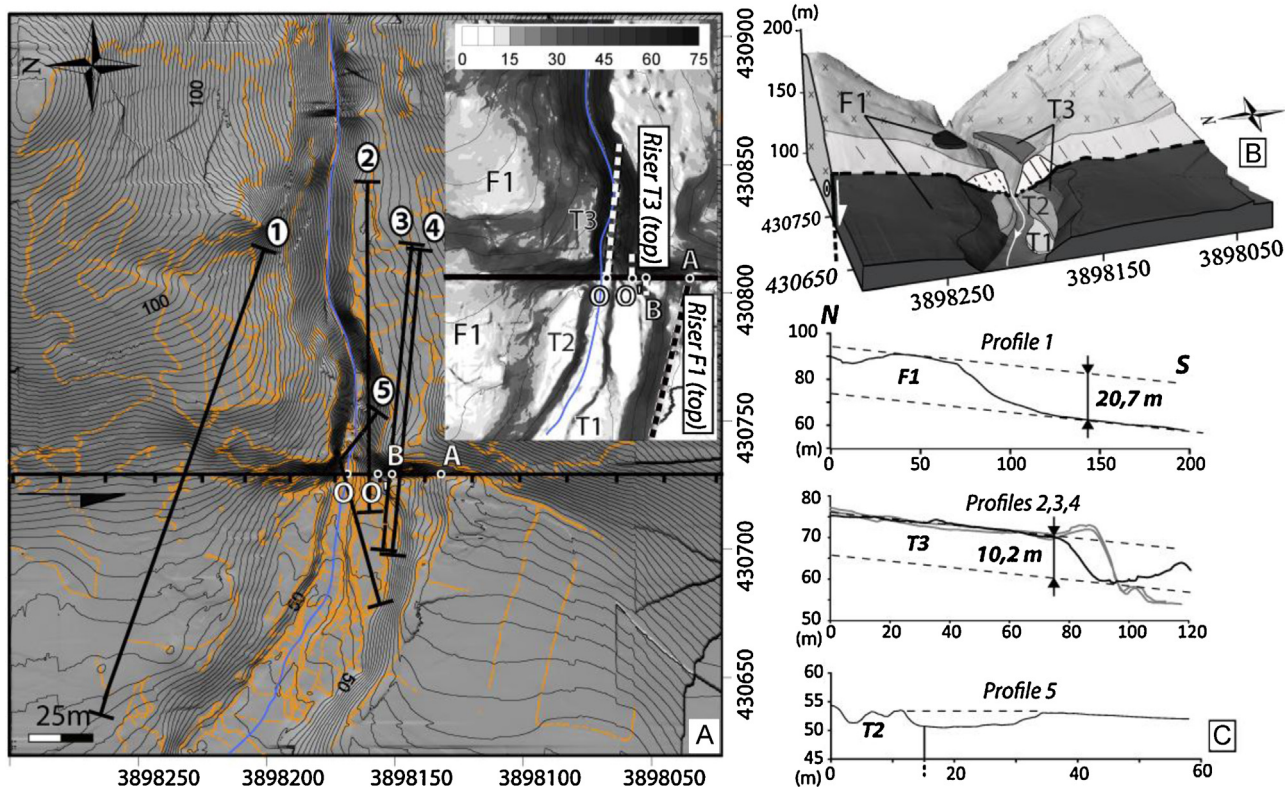


**Fig. 5.** (A) Digital Elevation Model (0.5 m grid) of the Trougout fault scarp with an interval contour of 1 m. Black line with ticks indicates the fault scarp; numbered black lines indicate location of the topographic profiles visible in (C). Top right: slope map of the fault scarp. Colors scale is given in degrees. Both markers were used to measure the offsets and are shown in dashed black lines for the top of the risers T2/T3 {A}, T3/F1 {B} and for the present {O} and the ancient {O'} riverbed. (B) 3D view of the DEM (0.5 m grid) of the fault scarp with the overlay geomorphologic interpretations. (C) Topographic profiles across the fault scarp showing the minimum vertical offset of the alluvial terraces.

These estimates of the vertical and horizontal components of displaced morphotectonics markers along the Trougout fault agree with a recent normal-left lateral strike slip displacement.

### 3.1.2. The Bou Haddad fault

South of the Ras Tarf massif, within the Ait Tessaft massif, we have observed a morphological feature that we interpret as a fault scarp, and that may corresponds to the southern extension of the Trougout fault (Figs. 2 and 6). This linear topographic scarp is clearly seen on the Google earth images, and the 1:30,000 scale aerial photographs (Fig. 7A and B). It is characterized by the abrupt stopping of eastwards dipping ridges and thalwegs along a N015°E trending scarp bounding a flat surface slightly tilted toward the east on which stands the Bou Haddad village. The southwards extension of the fault scarp is difficult to follow. The track of the fault disappears within a large landslide (Fig. 7B), south of which it crosses through several sigmoid streams along a line bending progressively toward the SW to reach the Nekor fault (Fig. 8A and D). This line passes through a well identified fault plane outcropping on the right riverbank of the oued Tarzout. It is characterized by a deformed zone displaying an outstanding slickenside on which striae indicate a horizontal displacement (Fig. 8B and C).

An E-W profile extracted from Spot 5 DEM across the cumulative scarp allows determining a difference of height of 36 m that would represent a minimum cumulative vertical offset associated with the normal displacement along the Bou Haddad fault (Fig. 7C). Within the main slope defining the large-scale cumulative scarp, small scarp features can be observed in few places (Figs. 7D and 9A). Although numerous artificial benches due to the agricultural activity can be found, we think that these features could correspond to the expression of a recent surface

rupture. We carried out a topographic survey with a RTK GPS of a site where the scarp is cutting through a small thalweg. The resulting DEM allows estimating a vertical offset of  $5.1 \pm 0.5$  m (Fig. 9B). There is no evidence for lateral displacement.

### 3.1.3. The Boudinar fault

The Boudinar fault corresponds to the fault bounding the Messinian to Quaternary Boudinar sedimentary basin to the West

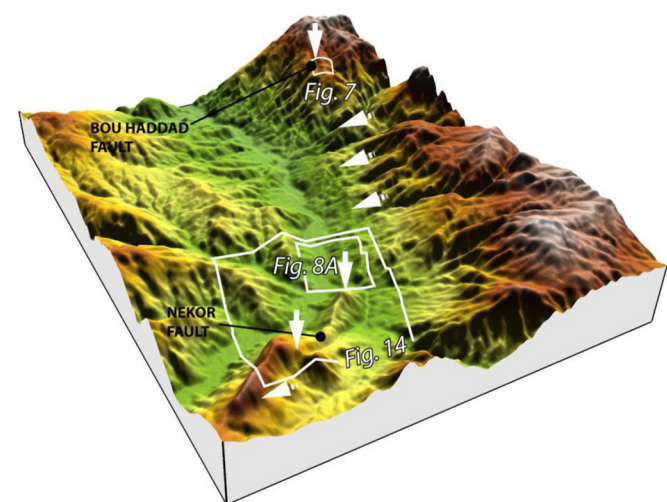


**Fig. 6.** DEM SPOT5 of the Nekor-Bou Haddad faults area. White arrows indicate the true fault scarp; white dashed arrows indicate the assumed fault trace. White squares indicate the study areas.

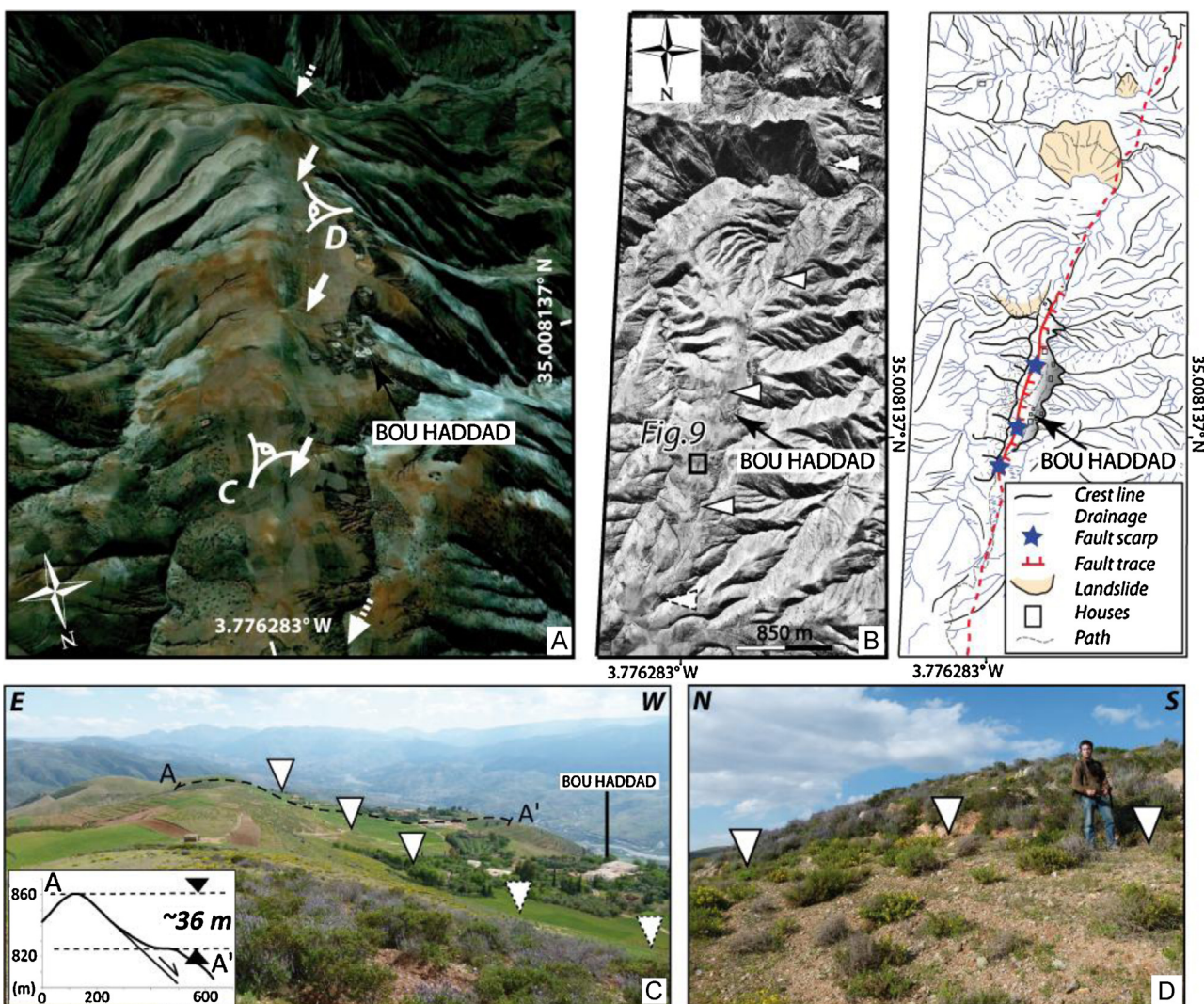


**Fig. 7.** (A) Perspective view of Google Earth image (<http://www.earth.google.com>) of the Trougout fault near the Bou Haddad village (35.008137°N; 3.776283°W). White arrows indicate the location of the fault. Note the deep incision on the eastern flank. (B) Aerial photograph (November 14, 2003) showing the fault trace (left) and the geomorphologic interpretation (right). White triangles point out the fault segment. Black squares indicate Fig. 9 location. (C) General overview of the study area and a topographic profile [A-A'] across the scarp showing the total vertical offset of the fault. The fault is represented by the white triangles. (D) Field view of the fault scarp showing a vertical offset. White triangles point out the base of the scarp; person on the hanging-wall gives the scale of the picture.

and limiting the Ras Tarf volcanic massif to the East (Fig. 2B). This ~25-km long structure is oriented roughly N-S with a N140°E short segment in its central part. Within this bended zone, the Messinian diatomites are dragged along the fault indicating a clear normal component (Fig. 10). An erosional marine surface located at ~150 m above the present mean sea-level (a.s.l) cuts the Messinian deposits, and stops against the fault scarp, here marked by an outstanding ~7 m sub-vertical free face cut through andesitic debris-flow deposits. Well-preserved striae are observed on the fault plane. The fault slip data measured on the fault plane are N140°E/76°E, with a pitch of 67°S indicating a dip-slip movement (normal) with a slight right-lateral component, consistent with the NE-SW transtension observed along the NS trending Trougout fault, at the other side of the Rastarf massif (see above) (Fig. 2B).

The geometry of the drag-fold and the constant thickness of the diatomite layers indicate a post-Messinian deformation. At its northern end, Quaternary marine terraces (see below) seal the fault suggesting that it is not active anymore.

### 3.1.4. The marine terraces of Al Hoceima and Ras Tarf

In the Al-Hoceima region and within the Ras Tarf cape, several Quaternary marine terraces ranging from 4 to 141 m a.s.l can be observed (Figs. 11–13). These terraces appear strongly weathered as shown by the development of rubified soil and calcretes. On 1:30,000 aerial photographs and Google Earth GeoEye images, several sand dunes intercalated between the marine terraces are observed defining whitish lines parallel to the present shoreline (Fig. 11A). Using kinematic GPS, we have carried out a 1.7 km-long NS topographic profile through the Iyya Tazaghine area, where the staircased morphology is well expressed. The profile shows three main slope breaks characterizing at least three marine surfaces located at  $12 \pm 1$  m,  $22 \pm 2$  m and  $80 \pm 5$  m a.s.l (Fig. 11A).

The lowest terrace (Tr1) situated  $12 \pm 1$  m a.s.l is observed all along the coast within the Ras Tarf cape and is characterized by a shallow-dipping planar surface marked by rounded decimetric pebbles and remains of marines shells embedded in a sandy matrix (Fig. 11B). Among the fauna, coral, *Patella safiana*, *Strombus* and marine gastropods can be found (Fig. 11C and D). We have also observed micro-boring on pebbles interpreted as marine

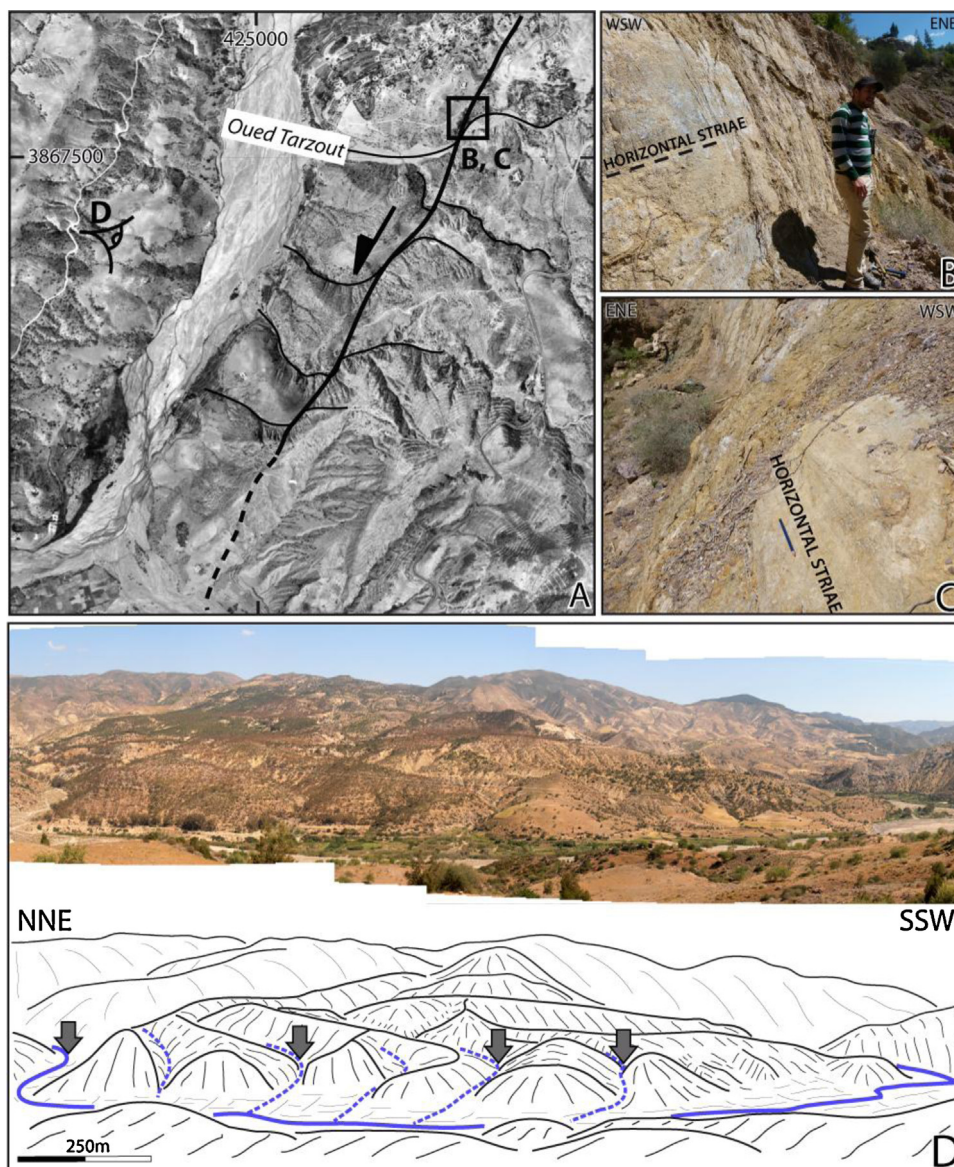


**Fig. 8.** (A) Aerial photograph (November 14, 2003) showing the fault trace at the junction between the Bou Haddad and the Nekor faults. Note the sigmoidal stream features along the fault trace. (B and C) Field view of the fault scarp showing the fault plane and the associated striae. (D) Field view and its interpretation of the fault zone. Gray arrows show the bending points of the sigmoid streams.

lithophagous fauna markers. The next terrace (Tr2) is situated at  $22 \pm 2$  m a.s.l with similar deposits than Tr1 (Fig. 12A). The third terrace (Tr3), situated at  $80 \pm 5$  m a.s.l., is characterized by a basal erosional surface covered by volcanic angular boulders (50 cm-diameter) embedded in a consolidated sand and bioclasts matrix (Fig. 12B and C). We interpret these boulders as screes deposited at the cliff foot of the paleo-shoreline. Among the bioclast matrix, we have found numerous shells of *Ostrea* sp., *Gibbula* sp., and *Cardium* sp. (Fig. 12D). Between Tr2 and Tr3, we observe a succession of dunes deposits characterized by consolidated sands containing continental shells. Remains of wave-cut platforms are marked on the topographic profile by slope breaks. However, non-marine sedimentary deposits were found within these surfaces. Continental deposits constituted of silty-clayed red sands and calcretes cover the overall morphology. A fourth marine terrace deposit (Tr4) is observed at  $141 \pm 5$  m a.s.l. and corresponds to the abrasive marine surface cutting through the Messinian deposits deformed by the Boudinar fault (Fig. 12E and F).

Within the Al-Hoceima area, two main marine terraces can be distinguished at 4 and 55 m a.s.l (Fig. 13A). The first one (Ta1) is observed along the Al-Hoceima coast either in the form of notches in the limestone and schist cliffs, or in the form of well-preserved planar surfaces made of cemented coarse sands and bioclasts (Fig. 13B). Among the bioclasts, *Gibbula* is the dominant specie. The second terrace is around 55 m a.s.l, being well characterized by a thick sandstone layer including pebbles showing trace-fossils due to benthic marine colored algae (*Rhodophyta*) and by remains of marines shells (e.g. *Pectinidae*) (Fig. 13C). The terrace is affected by numerous small normal faults, its elevation varying from +38 to +55 m a.s.l.

### 3.2. The jebel izra massif

#### 3.2.1. The Nekor fault

The Nekor fault probably corresponds to one of the major structures in the Rif during the Neogene period. However, its

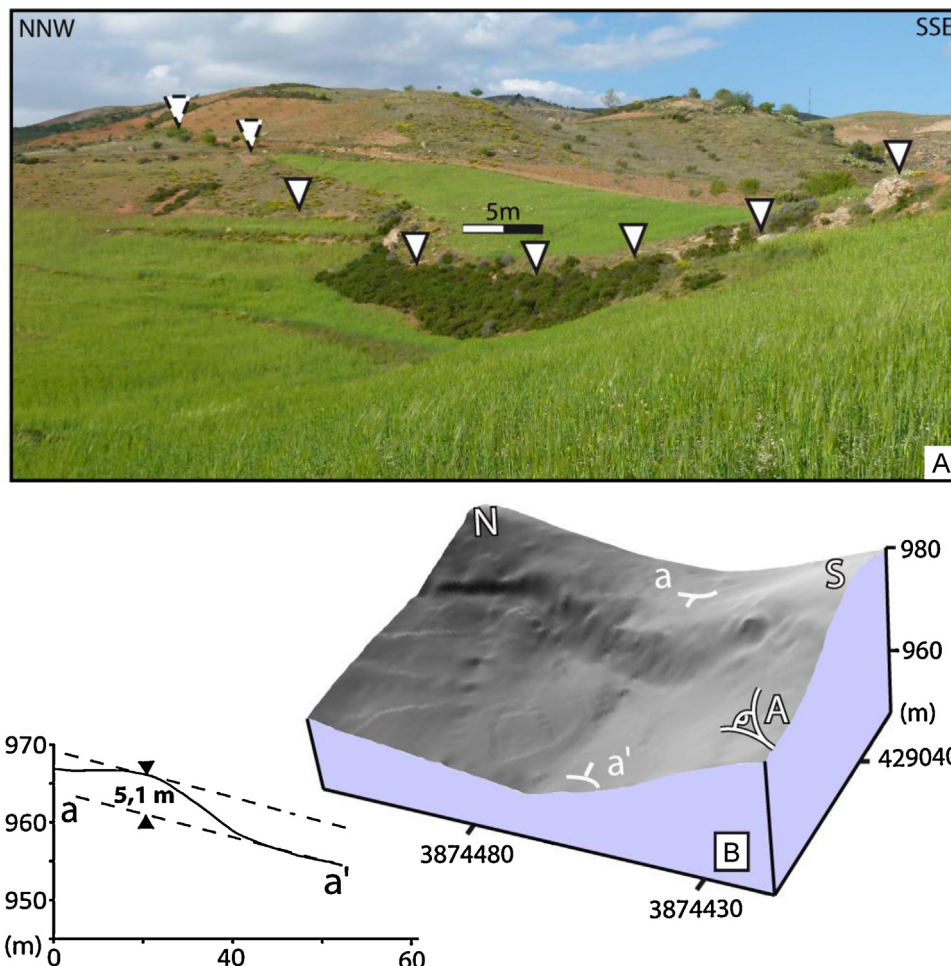


**Fig. 9.** (A) Field view of the fault scarp covered by vegetation. The tips of white triangles point out the top of the scarp. (B) 3D view of the Digital Elevation Model (1 m grid) of the fault scarp with location of a topographic profile {a-a'} across the scarp showing a vertical offset of 5.1 m.

present-day activity is not easy to demonstrate. Along the south-eastern border of the Boudinar basin (see Figs. 1A and 2B), the Nekor fault does not show any evidences of recent reactivation. But we have found some evidence of Quaternary activity

further west along a 10 km-long segment within the Jebel Izra (Fig. 14).

The first evidence is found on the southwestern flank of the massif (see location on Fig. 14). There, the fault trace is clearly seen in the



**Fig. 10.** Photograph of the drag folds along the Boudinar fault.

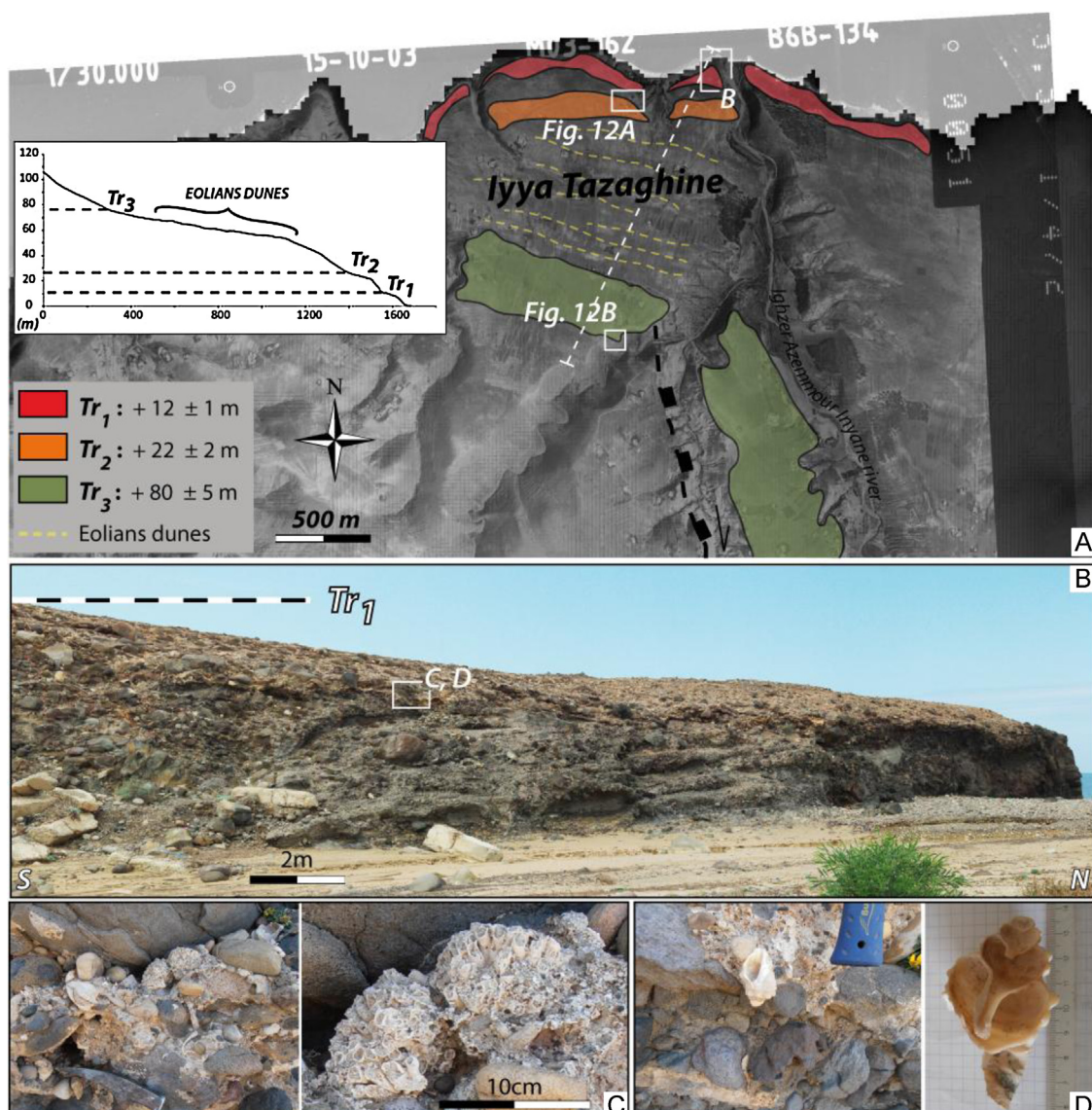


**Fig. 11.** (A) DEM (SPOT5) overlain by aerial photograph (October 15, 2003) of the Rastarf cape, field map of the location and extent of four marine terraces (from  $Tr_1$  to  $Tr_4$ ) and profile N-S across the marine surfaces. Black line with features indicates the north end of the West-Boudinar fault; colored surfaces correspond to the marine terraces; dashed yellow lines indicate location of the eolian dunes; white squares indicate the location of the study areas. (B) Field view, from the Igħżer Azemmour Iñyane river bed, of the marine terrace  $Tr_1$  located at  $+12 \pm 1$  m. Black and white line indicates location of the summit of the abraded marine surface; white square indicates the location of the shells sampled. (C) Photographs of corals sampled on the  $Tr_1$  terrace. (D) Field view and sectional view of a gastropod shell sampled on the  $Tr_1$  terrace. (For interpretation of the references to color in this figure legend, the reader is referred to the web version of the article.)

landscape as the tectonic contact between the Mio-Pliocene yellow marls to the NW, and a complex unit, Miocene in age, constituted of large limestone boulders included in mix of marls and gypsum, to the SE. Along this contact, we have observed several morphotectonics features suggesting that the fault is still active (Fig. 15). Two features allowed us to define the kinematics of the fault. The first one corresponds to a curved thalweg feature perched above a 30 m high and  $\sim 400$  m long cliff of limestone and gypsum corresponding to the fault contact (Fig. 15C1). The upstream and downstream parts of the thalweg appear beheaded by the fault and set 30 m above the main stream that incised the Neogene marls on the northwest side of the fault (Figs. 16A–C and 17). The second feature is observed 400 m to the northeast of the first one, and corresponds to a sigmoid stream feature along the fault contact (Fig. 15C2). We interpret these two features as evidences of recent left-lateral displacements along the fault. This interpretation is reinforced by a DEM from a GPS kinematic survey within the perched thalweg.

Fig. 17 shows clearly the 2 beheaded parts of the thalweg above the present stream that is now strongly incising the Neogene marls on the northwestern side of the fault contact. From the DEM, we estimate a  $42 \pm 5$  m cumulative horizontal displacement of the perched thalweg (Fig. 17). From the aerial photo, we estimate that the offset of the second drainage feature is about 25 m (Fig. 15C2).

#### 4. Geochronological data

##### 4.1. Cosmogenic $^3He$ dating of the trougout fault plane

###### 4.1.1. Methods

The principle of the cosmogenic  $^3He$  method of datation is based on the fact that the cosmic rays reach permanently the earth surface and their interactions with rocks create in situ cosmogenic isotopes. The longer the time the rocks are close to the surface, the longer they are submitted to the cosmic flux ray, and the higher



**Fig. 12.** (A) Sectional view along the coastal road located on the Rastarf cape of the  $Tr_2$  marine terrace. 1, 2: pictures of remaining marine shells visible in the marine terrace. Dashed white line indicates location of the summit of the terrace. (B) Field view from the south of the marine terrace  $Tr_3$ . Dashed white lines indicate the summit of the terrace  $Tr_3$ ; white square indicates location of the (C). (C) Photograph of marine deposits of the summit of  $Tr_3$ . The hammer gives the scale of the picture. (D) Photograph of remaining marine shells sampled on the summit of  $Tr_3$ . (E) Field view from the east of the marine terrace  $Tr_4$  near the Tigheza mosque (35.253224°N; 3.698029°W). Dashed line indicates the summit of the terrace, circled cows give the scale. (F) Photograph of remains of marine shells embedded in consolidated sand matrix of  $Tr_4$  terrace.

the in situ cosmogenic  $^3\text{He}$  concentration in their minerals (olivine and/or pyroxene) is. Thus, it is possible to date the time when the rocks were brought near the surface and study the processes that have emplaced them to the place where they have been sampled (e.g.: the deposit of alluvial material or the exposition of fault scarps due to earthquake cycle, Blard et al., 2005; Palumbo et al., 2004). In our case, seven samples (MA12-6A to MA12-6G), each constituted by amalgams of ~10–15 andesitic and basaltic clasts from pyroclastic breccia, were collected every 50 cm along the slip direction on the fault plane for the purpose of measuring their cosmogenic  $^3\text{He}$  contents (Table 1, Fig. 18). All samples are andesites and basalts from the Rastarf volcano that were emplaced more than 12 Ma (El Azzouzi et al., 1999; El Bakkali et al., 1998). These andesites and

basalts contain millimeter-size pyroxenes phenocrysts, a mineral well suited for cosmogenic  $^3\text{He}$  dating because it has a high helium retentivity (Blard et al., 2005; Trull and Kurz, 1993; Trull et al., 1991). The cosmogenic  $^{36}\text{Cl}$  method has been successfully applied to study the seismic cycle and estimate the slip rate of normal fault scarps cutting through limestone (e.g. Palumbo et al., 2004), but this is the first attempt to use the cosmogenic  $^3\text{He}$  method for a similar application on volcanic rocks.

All  $^3\text{He}$  and  $^4\text{He}$  concentrations were measured at the CRPG noble gas lab, using the SFT mass spectrometer by GV and following the procedures previously described in (Blard et al., 2013). To obtain pure separates of pyroxenes, samples were crushed and sieved, and the 100–200  $\mu\text{m}$  fraction was separated in heavy liquid. Most of

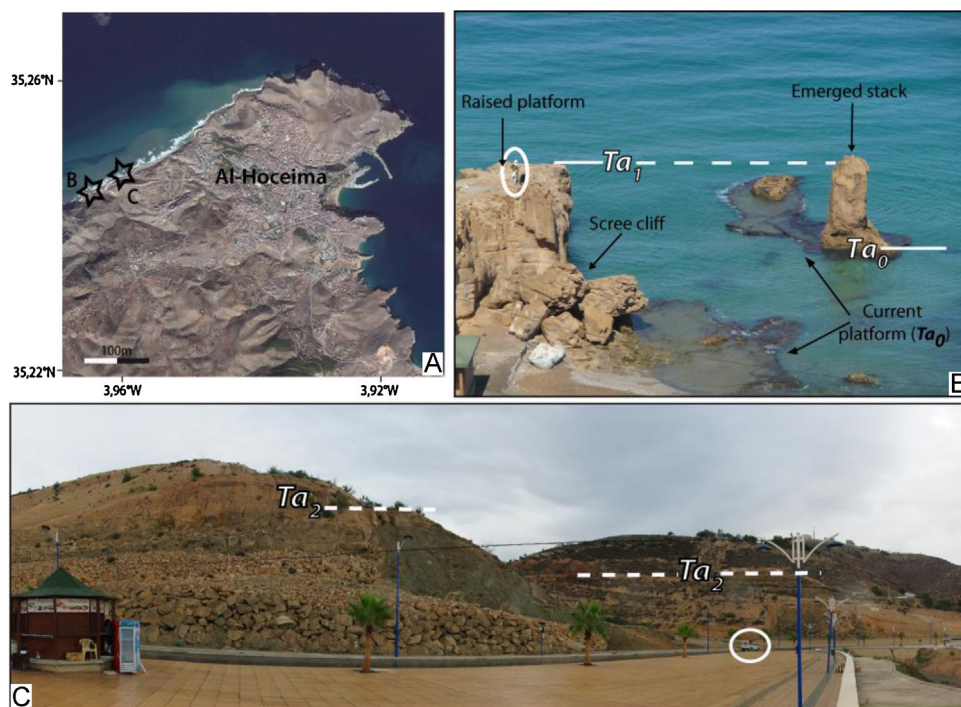


**Fig. 13.** (A) Plan view of satellite image (Google Earth) of the Al-Hoceima cape. Red stars indicate location of the places where the marine terraces were observed. (B) Field view of the actual ( $Ta_0$ ) and the previous marine terrace ( $Ta_1$ ) along the western Al-Hoceima coastline (photo by R. Leroux-Mallouf). White lines point out the summit of the terraces; the circled person gives the scale of the picture. (C) Panoramic view from the coast road west of Al-Hoceima city (photo by R. Leroux-Mallouf). The summit of the third marine terrace observed on Al-Hoceima coastline, named  $Ta_2$ , is indicated by dashed white line. It crops out at +55 m above sea level and appears as a 1 m-thick indurated sand layer surrounded by continental deposits.

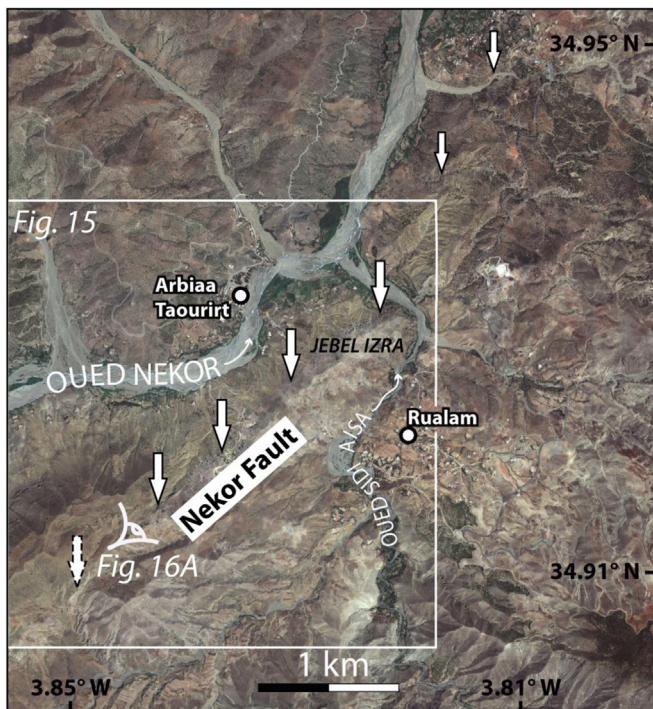


**Fig. 14.** Plan view of Google Earth image of the Nekor fault. White arrows indicate the location of the fault mapped during field investigations; dashed arrows indicate the likely continuity of the fault; white dots indicate location of the villages; white square indicates location of the study area.

these pyroxene grains were pure and had no melt or mineral inclusions. The magmatic  $^3\text{He}$  and  $^4\text{He}$  concentrations were determined by in vacuo step-crushing (from 1 to 15 min) of pyroxenes aliquots (Kurz, 1986; Scarsi, 2000). To extract all cosmogenic  $^3\text{He}$ , uncrushed phenocrysts were fused in vacuo during 15 min at 1400 °C, in a new custom single vacuum furnace (Zimmermann et al., 2012). After gas purification, the total  $^3\text{He}$  and  $^4\text{He}$  concentrations were analyzed with the SFT mass spectrometer. The build-up of nucleogenic  $^3\text{He}$  was calculated using major and traces elements measured in phenocrysts and in bulk rocks. Cosmogenic  $^3\text{He}$  data and calculated exposure ages are given in Table 1.

#### 4.1.2. Estimating exposure ages of the Trougout fault

In order to quantify the slip rate along the fault, we sampled the alluvial deposits within the fan F1 and the terrace T3, and the outcropping fault plane to estimate their surface age exposure using in situ cosmogenic  $^3\text{He}$ . Analyses of samples collected within the terraces are in progress in CRPG Nancy. We present here the results obtained within the fault plane (Fig. 18 and Table 1). The cosmogenic  $^3\text{He}$  surface concentrations of the 7 samples collected along a 3 m long section of the fault plane parallel to the slickensides show a general growing trend from  $2.29 \pm 0.93 \times 10^5$  at/gr within the ground surface (sample 6G) to  $4.86 \pm 0.76 \times 10^5$  at/gr (sample 6A) at 2 m above the ground surface (3 m from sample 6G along a line parallel to the slickensides) (Fig. 18A and Table 1). This trend is consistent with the normal-left-lateral kinematics observed along the fault with growing concentrations from the bottom to the top of the fault plane.

The distribution of concentrations along the fault plane may be interpreted as (i) 2 main clusters suggesting that its exposure occurred in two stages, which in turn suggests two coseismic displacements or (ii) a constant growing trend which suggests few successive events with low coseismic displacements (<50 cm). In the case (i), the mean concentrations of the 2 clusters are

Sample	Height of samples from the ground (cm)	Altitude (m)	Latitude, °N	Longitude, °E	Number of clasts sampled in the fault plane breccia	Clasts thickness (cm)	Mineral	Sample size (μm)	Mass (mg)	${}^4\text{He}$ ( $10^{-12}$ at g $^{-1}$ )	${}^3\text{He}$ ( $10^{-3}$ at g $^{-1}$ )	Uncertainty ( $\pm\sigma$ ) (10 $5$ at g $^{-1}$ )	Assuming that there are two main clusters				
													Mean concentrations ( $10^5$ at gr $^{-1}$ )	Uncertainty ( $\pm\sigma$ ), ( $10^5$ at gr $^{-1}$ )	Age ( $\pm\sigma$ ), yr		
MA12-6A	300	62	35.224	3.76126	12	~5	Pyroxène	100–200	567.6	3.74	4.86	0.76	62.7	7.75	1.21	7190	1240
MA12-6B	250	61.5	35.224	3.76126	11	~4	Pyroxène	100–200	577.2	3.56	3.68	0.87	62.7	5.87	1.14		
MA12-6C	200	61	35.224	3.76126	9	~5	Pyroxène	100–200	538	3.4	4.99	0.71	62.7	7.97	1.13		
MA12-6D	150	60.5	35.224	3.76126	8	~5	Pyroxène	100–200	363.7	3.73	1.76	1.21	62.7	2.81	1.92	2.52	1840
MA12-6E	100	60	35.224	3.76126	10	~3	Pyroxène	100–200	251.4	3.2	3.52	1.33	62.7	5.62	2.12	1.15	4030
MA12-6F <sup>a</sup>	50	59.5	35.224	3.7613	7	~5	Pyroxène	100–200	408.8	3.51	5.23	0.73	62.7	8.34	1.17		
MA12-6G	0	59	35.224	3.76126	10	~5	Pyroxène	100–200	401.3	3.79	2.29	0.93	62.7	3.65	1.49		

According to the hypothesis (i), samples MA12-6A to -6C has been considered as belonging to a first cluster, and samples MA12-6D to -6G to a second cluster (see text for more details).  
<sup>a</sup> MA12-6F is considered as an outlier and has not been taken into account for the calculations of the mean concentrations of the second cluster (MA12-6D to MA12-6G). Production rate ( $P_0$ ) has been determined using the SLHL P3 value of  $125 \pm 5$  at/gr/yr (Blard et al., 2013) and the parameters of Stone (2000).

$4.51 \pm 0.78 \times 10^5$  at/gr and  $2.52 \pm 0.11 \times 10^5$  at/gr, respectively (Fig. 18C and Table 1).

To calculate the corresponding surface ages, we first calculated the local production rate of in situ produced  ${}^3\text{He}$  at surface using a sea level and high latitude (SLHL) P3 value of  $125 \pm 5$  at/gr/yr (Blard et al., 2013) and the altitude- and latitude-dependant polynomials of (Stone, 2000). We obtained a value of 105 at/gr/yr. Because the samples are partially shielded from the cosmic-ray flux by the sub-vertical fault plane (dip  $80^\circ$ ) and the riser between T3 terrace and F1 fan surface (dip  $35^\circ$ ) (Fig. 18B), we applied to this production rate a correction factor (Greg Balco, [http://hess.ess.washington.edu/math/general/skyline\\_input.php](http://hess.ess.washington.edu/math/general/skyline_input.php), Version 1.1. March, 2006) to obtain a corrected production rate ( $P_0$ ) of 62.7 at/gr/yr.

In the case (i), this yields the mean ages of  $4.03 \pm 1.84$  ka and  $7.19 \pm 1.24$  ka for the 2 seismic events, respectively (considering that there is no inherited  ${}^3\text{He}$  associated with pre-exposure). These results suggest that the two seismic events were separated by a period of time of  $3.16 \pm 1.54$  ka and that the average slip rate along the fault is  $0.95 \pm 0.47$  mm/yr. This corresponds to a horizontal left-lateral component of  $0.47 \pm 0.23$  mm/yr, a vertical component of  $0.82 \pm 0.31$  mm/yr and an extensional rate, perpendicular to the fault, of  $0.12 \pm 0.05$  mm/yr. In the case (ii), using the same production rate ( $P_0$ ) and the difference between the fault bottom age and the fault top age or the linear regressive slope of the growing trend, we obtain a period of time of  $4.1 \pm 1.35$  ka. This corresponds to an average slip rate along the fault of  $0.73 \pm 0.3$  mm/yr, a horizontal left-lateral component of  $0.36 \pm 0.15$  mm/yr, a vertical component of  $0.63 \pm 0.25$  mm/yr and an extensional rate of  $0.11 \pm 0.04$  mm/yr. However, we emphasize that these results are really preliminary and should be considered with caution. Further sampling for  ${}^3\text{He}$  dating should be conducted along the whole fault scarp to sample several earthquake cycles.

#### 4.2. U/Th analysis

##### 4.2.1. Analytical techniques

The mollusc shell or coral fragments were first treated with a drill to remove altered or impure parts, then ultrasonically cleaned in distilled water. Two to four grams of carbonate were used for the analyses. Some samples were crushed and heated in a furnace at  $550^\circ\text{C}$  for several hours in order to eliminate the organic matter, and then dissolved in nitric acid, after addition of a  ${}^{232}\text{U}$ - ${}^{228}\text{Th}$  tracer. Other samples were directly spiked, dissolved in nitric acid and left overnight on a hot plate ( $\sim 80^\circ\text{C}$ ). The solutions are then evaporated to incipient dryness, and the residue dissolved in diluted nitric acid. After addition of 5–10 mg Fe as iron nitrate, the iron hydroxide (with U and Th isotopes) is precipitated with  $\text{NH}_4\text{OH}$ . The precipitate is centrifuged, rinsed with distilled water, and dissolved in  $\text{HNO}_3$ . The solution is evaporated to dryness, and the residue dissolved in 2–3 ml of  $\text{HNO}_3$  7N.

U and Th are then purified on two successive columns (10 ml and 1.5 ml, respectively) filled with AG1 X8 anionic resin conditioned with  $\text{HNO}_3$  7N. U and Th are eluted with  $\text{H}_2\text{O}$  and HCl 8N, respectively. After evaporation, the residue is dissolved in 0.5 ml of HCl 8N, and the separation of U and Th is achieved on a 0.5 ml column of AG1X8 resin conditioned in HCl 8N. U is retained on the resin, while Th passes through and is collected. U is finally eluted with  $\text{H}_2\text{O}$ .

After evaporation, U and Th fractions are dissolved in an ammonium sulphate solution at pH~2 and separately electroplated on polished stainless steel disks according to the method described by Talvitie (1972). The disks are then introduced and counted in a 576A dual alpha spectrometer (ORTEC<sup>TM</sup>) equipped with ULTRATM ion implanted silicon detectors.

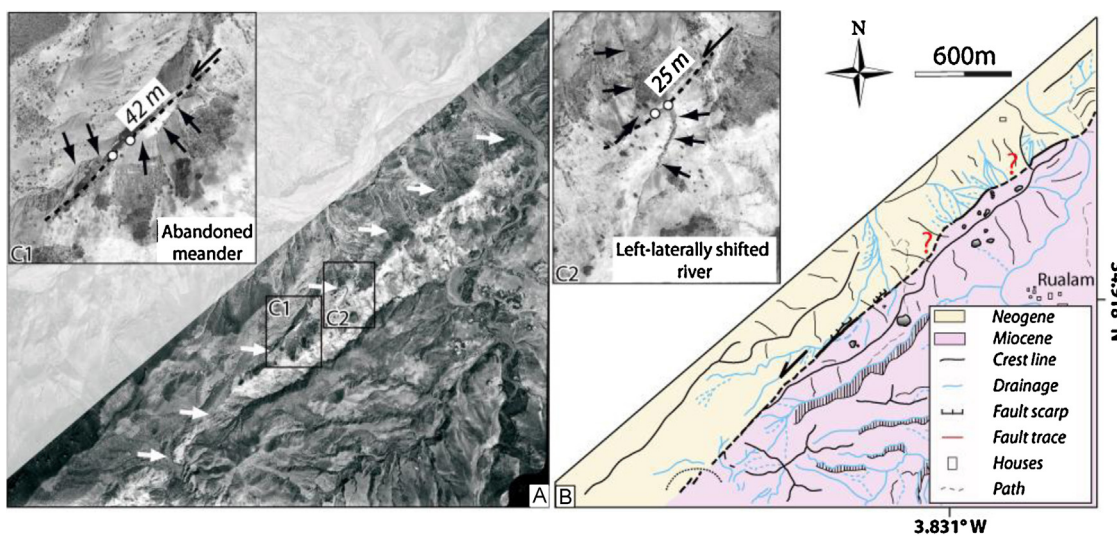


**Fig. 15.** (A) Aerial photograph of the Nekor fault along the Jebel Izra. White arrows point out the fault scarp; rectangles with black boundaries and labels indicate location of the pictures C1 and C2. (B) Geomorphologic interpretation of the aerial photograph. (C1 and C2) Enlarged pictures of aerial photo showing the morphologic markers of the fault displacement.

#### 4.2.2. U-Th ages of marine terraces within the Ras Tarf Cape

We have attempted to date Tr1 and Tr3 terraces located at +12 and +80 m a.s.l respectively, through the U-Th method on mollusc shells (Figs. 11C, D and 12D). However, since early works in this domain (e.g. Kaufman et al., 1971; Stearns and Thurber, 1965), it is well known that mollusc shells often behave as open-systems for U-Th dating. Moreover, there are no a priori criteria to assess the validity of the ages obtained (such as the U content, the  $(^{234}\text{U}/^{238}\text{U})$  activity ratio or the calcite/aragonite proportion). Several authors have reported U-Th ages that are much younger than the well-established age, based on paleontological and morphological

criteria (e.g. Choukri et al., 2011, 2007; Meghraoui et al., 1996; Zazo et al., 1999). In their detailed study on 75 samples of mollusc shells from the ~120 ka (MIS 5e) marine terrace along the Atlantic coast of Morocco, Choukri et al. (2011) obtained ages as young as 40 ka. However, only one sample showed an age slightly older than the 120 ka. About 30% of the samples analyzed gave ages compatible with 120 ka, within analytical uncertainties, whatever their  $(^{234}\text{U}/^{238}\text{U})$  ratio, which are sometimes much higher than expected for a marine shell evolving in a closed system [ $(^{234}\text{U}/^{238}\text{U}) \leq 1.15$ ]. This suggests that the samples dated at ~120 ka underwent an U-enrichment (with a high "continental"  $(^{234}\text{U}/^{238}\text{U})$  ratio) shortly

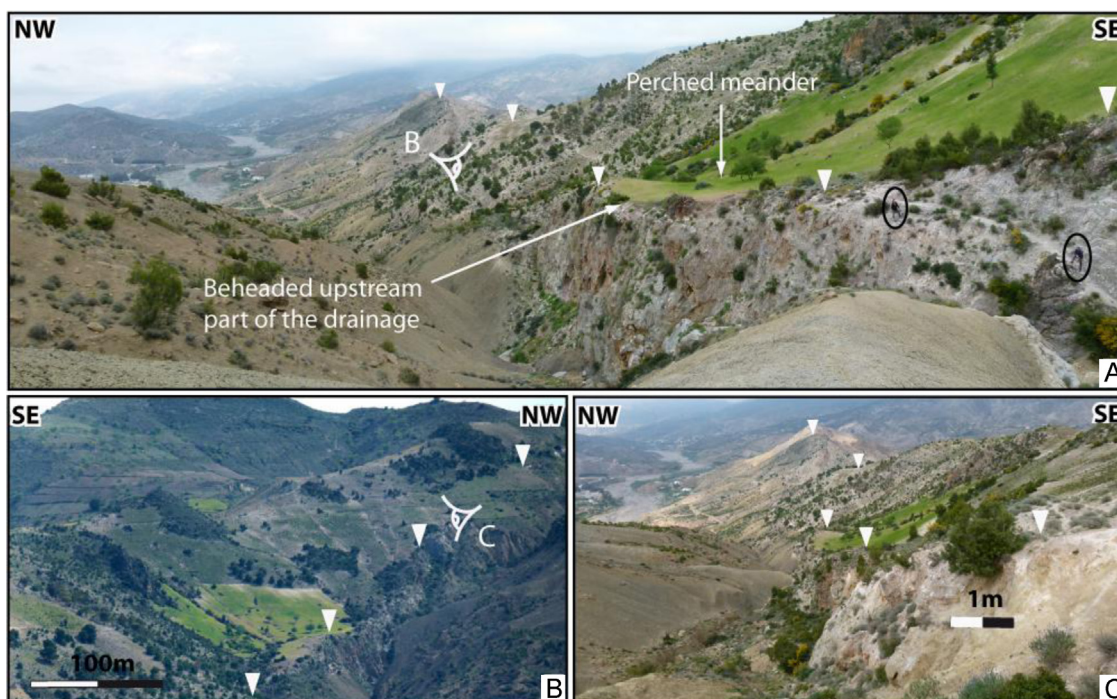


**Fig. 16.** (A) Field view from the SW of the Nekor fault scarp affecting quaternary alluvial surface (see text for more details). White triangles point out the fault scarp and the circled person gives the scale of the picture. (B and C) Field views from the SW and NE, respectively, of the Nekor fault scarp affecting the Messinian gypsum (that corresponds to the cliff) and the Neogene yellow marls of the Jebel Izra. White triangles point out the fault.

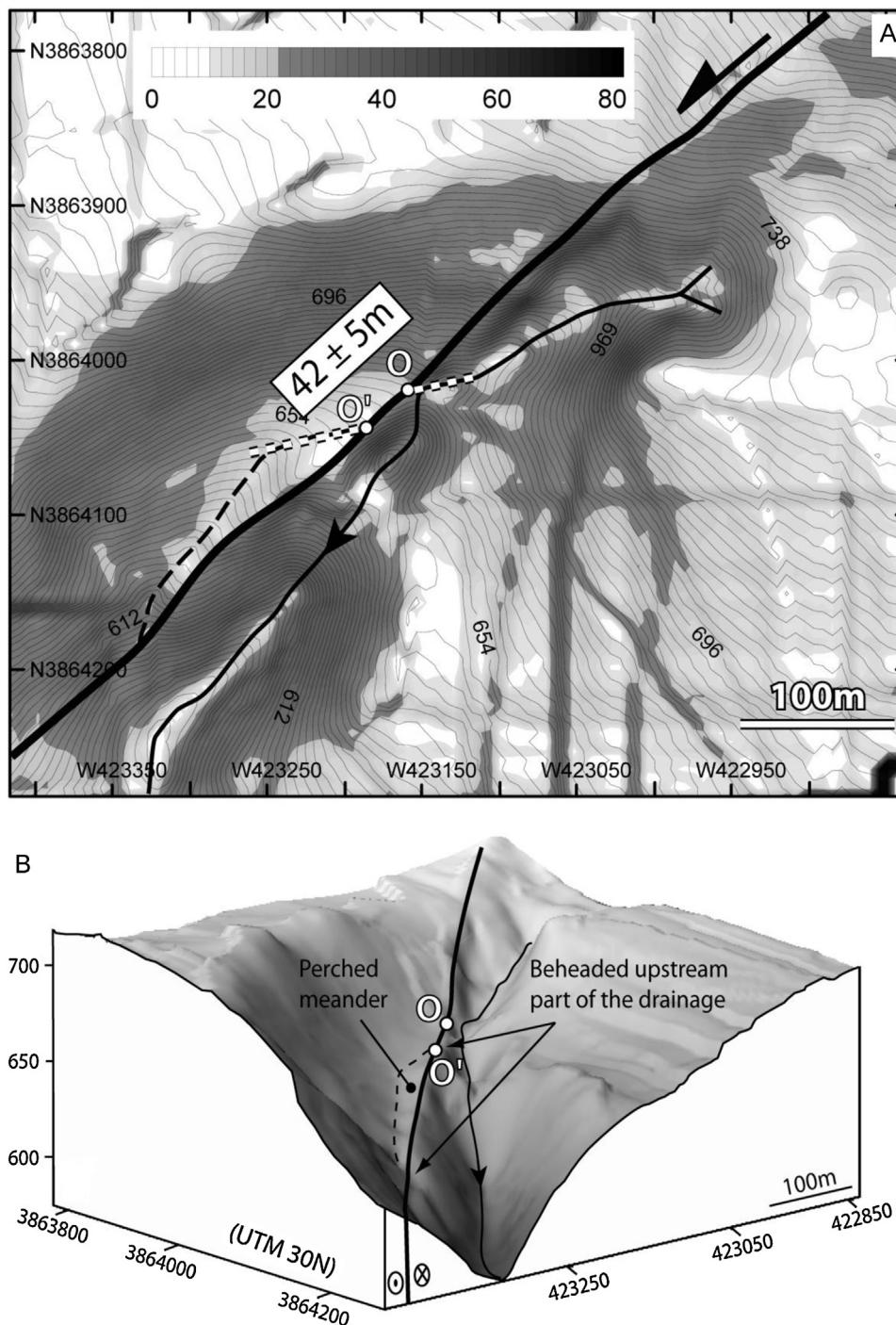


**Fig. 17.** (A) Slope map of the Nekor fault scarp. Colors scale is given in degrees. Black line indicates the fault scarp. Both markers were used to measure the offset and are shown by dashed black lines for the present stream direction {O} and the beheaded upstream part of the drainage {O'}. (B) 3D view of the Digital Elevation Model (1 m grid) of the fault scarp with location of the fault, the piercing points used to estimate the offset and the main stream.

after the death of the mollusc and the emergence of the terrace. Thus, it seems reasonable to lend some credit only to the oldest ages found for mollusc shells of a given terrace.

We have analyzed 11 samples or sub-samples using standard chemical procedures for U-Th separation, and alpha-spectrometry. Data are reported in Table 2, and in the classical ( $^{234}\text{U}/^{238}\text{U}$ )–( $^{230}\text{Th}/^{238}\text{U}$ ) diagram (Fig. 19A). None of the samples plot on the closed-system evolution curve, starting with the initial ( $^{234}\text{U}/^{238}\text{U}$ )<sub>0</sub> ratio of seawater (1.15) instead, all of them have experienced variable open-system exchanges.

Two sub-samples from both a coral fragment and a gastropod shell (*Strombus*) from the Tr1 terrace yield ages around 200 ka (Fig. 19A), while two *Cardium* shells display very young ages of around 50 ka. The age of 200 ka suggested by our data for the Tr1 terrace can be considered as surprising since this terrace is often assumed to correspond to the latest interglacial period at ~120 ka along the coasts of Morocco (the so-called Ouljian stage corresponding to MIS 5e).

The five samples from Tr3 terrace clearly give much older ages, although two of them (O2 and O6-3) seem again shifted toward

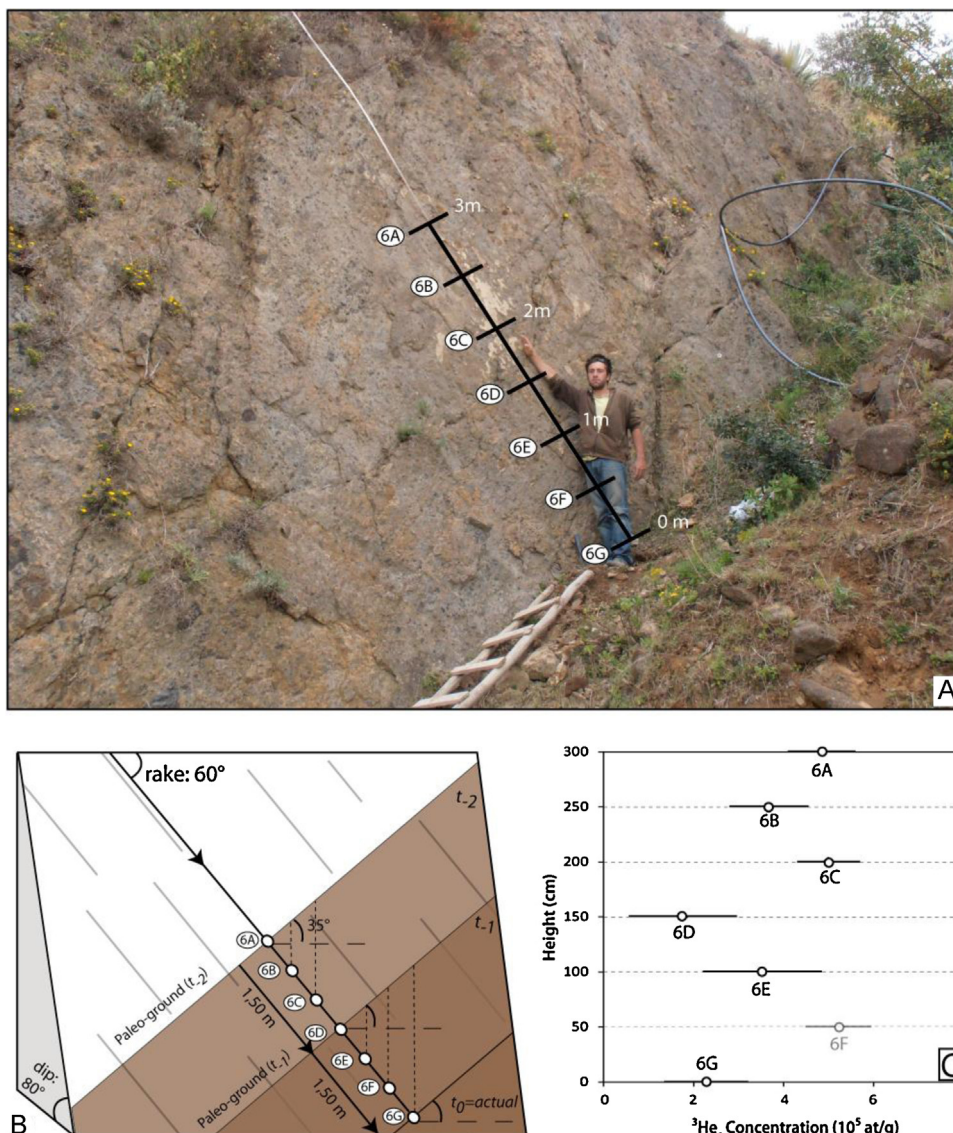


**Fig. 18.** (A) Photograph of the Trougout fault plane sampled along the slickenslides. The person gives the scale and shows the slickenslides direction. Note the 35°-dipping of the ground corresponding to the riser between T3 terrace and F1 fan surface. (B) Sketch representing the fault plane with the samples aligned along the slickenslides. Brown areas represent the partial shields from the cosmic-ray flux (see text for more details) by the riser F1-T3 (dip 35°). According to the hypothesis (i), we consider two events with a coseismic displacement of 1.50 m along the slickenslides (see text for further details). (C) Height profile of the  ${}^3\text{He}$  distribution along the fault plane.

**Table 2**  
U-Th data (alpha spectrometry).

Samples	U (ppm)	Th (ppm)	$({}^{234}\text{U})/({}^{238}\text{U})$	$({}^{230}\text{Th})/({}^{238}\text{U})$	Age (ka)
Upper terrace (80 m)					
O1 (Ostrea)	0.129	0.001	$1.105 \pm 0.031$	$1.146 \pm 0.039$	<b>461 (+340–160)</b>
O2 (Ostrea)*	0.160	0.003	$1.216 \pm 0.038$	$1.160 \pm 0.050$	268 (+100–60)
G (Gibbula)	0.339	0.047	$1.253 \pm 0.016$	$1.305 \pm 0.034$	<b>404 (+230–110)</b>
C6-2 (Cardium)	2.30	0.024	$1.419 \pm 0.029$	$1.537 \pm 0.062$	<b>426 (+300–140)</b>
O3 (Ostrea)*	0.197	0.017	$1.152 \pm 0.036$	$1.079 \pm 0.039$	261 (+93–55)
Lower terrace (12 m)					
S1 (Strombus)	0.876	0.008	$1.232 \pm 0.027$	$1.085 \pm 0.036$	<b>203 (+34–27)</b>
S2 (Strombus)	0.864	0.011	$1.273 \pm 0.015$	$1.090 \pm 0.026$	<b>186 (+20–18)</b>
Co1 (Coral)	1.82	0.287	$1.108 \pm 0.016$	$0.971 \pm 0.025$	<b>213 (+35–28)</b>
Co2 (Coral)	1.63	0.286	$1.101 \pm 0.024$	$0.953 \pm 0.035$	<b>207 (+51–36)</b>
C8-1 (Cardium)*	2.86	0.006	$1.327 \pm 0.016$	$0.451 \pm 0.014$	44.5 (+3.1–3)
C8-4 (Cardium)*	1.54	0.013	$1.350 \pm 0.015$	$0.551 \pm 0.014$	55.9 (+3.2–3.1)

Reported errors on activity ratios are  $1\sigma$  errors. However age uncertainties were calculated at  $2\sigma$  level, using the Monte Carlo method implemented by Ludwig in the Isoplot program (Ludwig, 2003, 2012). Sample marked with an asterisk (\*) are thought to give unreliable ages (see text for explanation). Ages in bold characters are those assumed to be the most reliable.

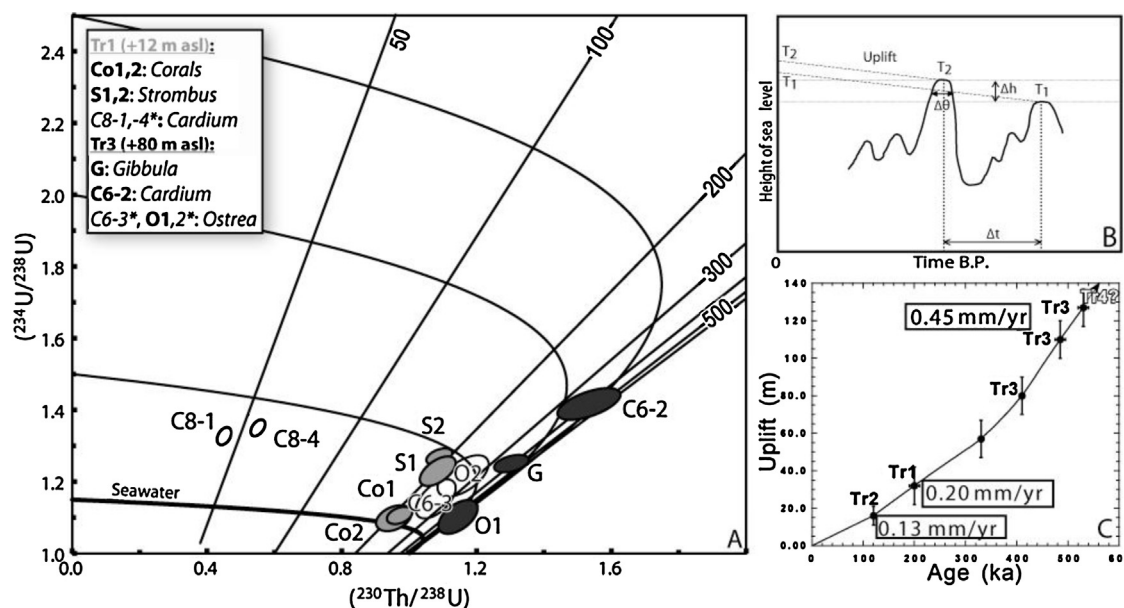


**Fig. 19.** (A) Data from the lower (+12 m) and upper (+80 m) terraces reported in the  $(^{230}\text{Th}/^{238}\text{U})$ – $(^{234}\text{U}/^{238}\text{U})$  diagram. Four evolution curves corresponding to  $(^{234}\text{U}/^{238}\text{U})$  initial ratios of 1.15 (seawater value), 1.5, 2 and 2.5 are reported in the diagram, together with several isochrons (ages in ka). For clarity, error ellipses are plotted at 68.3% confidence level, using the Isoplot program for U-Th data (Ludwig, 2012, 2003). Light-gray filled ellipses correspond to data for the upper terrace, dark-gray ones to data for the lower terrace. Open ellipses correspond to sample whose ages are thought unreliable (see text for discussion). (B) Schematic illustration of the case where a younger terrace (T2) can be found at a higher altitude than an older one (T1). In this example, the uplift rate  $u$  is such that  $u \cdot \Delta t < \Delta h$  (see text for explanation). (C) Hypothetical evolution of the uplift rate with time (in mm/yr) in the Ras Tarf area (see text for explanation). Uplift (in m) is calculated as the difference between the present-day altitude of a terrace and the height of sea-level at the time of its formation. Errors bars on ages correspond to the approximate duration of successive high-stands, while those on uplift derive from the uncertainties in the sea-level curve of Bintanja et al. (2005).

biased younger ages. The data suggest that the three other samples could be 400–600 ka-old, at the limit of the U-Th method based on alpha-spectrometry data (Fig. 19A).

Therefore, we consider, in the following discussion, the ages of 200 ka for Tr1 terrace and 400–600 ka for Tr3 terraces.

#### 4.2.3. Uplift rates along the Ras Tarf cape

The discussion below is based on the usual assumption that marine terraces correspond to sea-level high-stands (Anderson et al., 1999; Chappell and Shackleton, 1986; Zazo et al., 1993; Bradley and Griggs, 1976; Plaziat et al., 2008), which might not be always the case. However, the fossil macrofauna found on the well-identified terraces of this area are characteristic of warm water (e.g. *Strombus*, corals). The common model assuming that the age of marine terraces increases with their height a.s.l. is certainly valid in regions of high uplift rates (e.g.  $>0.5$  mm/yr). However, this might not be true in areas with moderate or low uplift rates. This is illustrated in Fig. 19B where a portion of the global sea-level curve is plotted, showing two successive high-stands, with the younger one reaching a higher level than the previous one. If  $\Delta h$  (in m) represents the difference in sea level between these successive high-stands,  $\Delta t$  their age difference (in ka), and  $u$ , the uplift rate (in m/ka, or mm/yr), assumed constant in this example, then three different models can be envisioned: (i) if  $u \cdot \Delta t > \Delta h$ , the older terrace will be above the younger one when both are uplifted above sea-level, which corresponds to the usual model; (ii) if  $u \cdot \Delta t < \Delta h$ , the older terrace will be at a lower altitude than the younger one when both are emerged. Note that the older terrace will remain submerged within the interval  $\Delta\theta$  (Fig. 19B), usually only for a few thousands of years, a duration probably not long enough to erase this terrace by submarine erosion; (iii) when  $u \cdot \Delta t \sim \Delta h$ , a composite terrace or two terraces very close in altitude, corresponding to the two successive high-stands will result. In a succession of more than two high-stands, with progressively higher sea levels, a series

of closely spaced terraces can be produced, even if they have rather large age differences.

We suggest that the age of 200 ka for terrace Tr1 (+12 m), deduced from our U-Th data, corresponds to MIS 7. The 120 ka high-stand (MIS 5e), which is usually well marked in the morphology, should then correspond to the terrace Tr2, located at +22 m, according to model (ii). Considering the sea level curve given by Bintanja et al. (2005) (+6 m height for the MIS 5e high-stand and  $\sim -20$  m for the MIS 7), this yields an average uplift rate of 0.16 mm/yr since 200 ka (0.2 mm/yr between 200 ka and 120 ka, and 0.13 mm/yr since 120 ka).

The older high-stand at 330 ka (MIS 9) is probably not represented by a true terrace with marine deposits. But it could correspond to one of the succession of breaks of slope found between Tr2 and Tr3 which can be interpreted as remains of marine terraces. Note that, if the 330 ka high-stand was represented by the Tr2 terrace, this would imply, based on the Bintanja et al.'s (2005) curve, a subsidence between 330 ka and 200 ka, a rather unlikely scenario.

The ages found on terrace Tr3 (400–600 ka) are affected by rather large uncertainties that preclude their attribution to a precise Isotope Stage. But this terrace could well correspond to a composite terrace according to model (iii), since three successive high-stands (belonging to MIS 11, 13 at around 410, 485 and 530 ka) seem characterized by increasing sea-levels after Bintanja's curve (Bintanja et al., 2005). If Tr3 is indeed a composite terrace, the calculated uplift rate would be 0.45 mm/yr between 410 and 530 ka. Note that, with an uplift rate of 0.45 mm/yr, one would expect that the high-stand of MIS 15 at  $\sim$ 600 ka could be represented by a terrace at  $\sim$ 140 m altitude, which is indeed present in the Ras Tarf region (see above).

Fig. 19C summarizes our interpretations. Although this figure should be taken with caution in view of the presently available data, it nevertheless suggests a regularly decreasing uplift rate, from about 0.45 mm/yr 500 ka ago, to 0.2 mm/yr between 200 and 120 ka

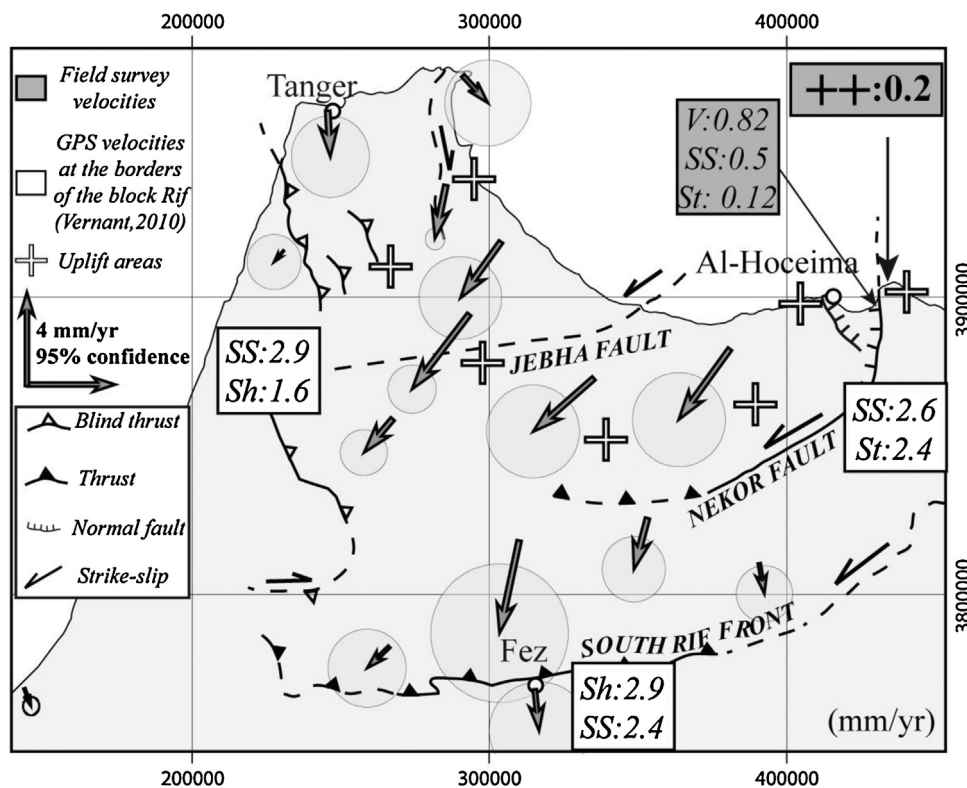


**Fig. 20.** Sketch map of active deformation within the Rif mountains (SS: strike-slip, V: vertical, St: stretching and Sh: shortening components) and GPS sites velocities. Black lines indicate strike-slip, reverse (with triangles) or normal (with ticks) faults observed on the field; dashed lines indicate faults drawn after the geological map of Morocco; white dots: main cities. Uplifted areas are reported from field observations (NE and central Rif) and from El Kadiri et al. (2010) (NW and Mediterranean shoreline).

ago, and to 0.13 mm/yr since 120 ka. These moderate uplift rates are not uncommon in the West Mediterranean region (El Kadiri et al., 2010; Meghraoui et al., 1996; Zazo et al., 1999).

## 5. Discussion

The new morphotectonic and geochronological data provided in this study point out the main active fault zones in the Northeastern Rif. Using U-Th ages of uplifted marine terraces we estimate an average uplift rate of the Ras Tarf of ~0.2 mm/yr since 500 ka in agreement with previous studies (Meghraoui et al., 1996; Morel and Meghraoui, 1996). Bounding the Ras Tarf to the west, the Trougout fault has a normal and left-lateral slip. The cosmogenic <sup>3</sup>He analysis along the fault plane suggests a slip rate over the last ~7190 ± 1240 years of ~0.73–0.95 mm/yr, with vertical and horizontal components of ~0.63–0.82 mm/yr and ~0.36–0.47 mm/yr, respectively. Although preliminary, the <sup>3</sup>He analysis suggests a return period of 3.1 kyr for the earthquakes rupturing the surface. Both the length of the fault segment (40 km) and the average earthquake displacement (1–1.5 m) suggest magnitudes of 6.5–7 (Wells and Coppersmith, 1994), which are higher than the instrumental seismicity reported in this region. The Trougout fault kinematics and the uplift rate of the Ras Tarf imply subsidence of the Al Hoceima bay with a rate of at least 0.5 mm/yr. This is consistent with the 400 m of Quaternary sediments reported in the bay based on hydrogeological drilling (Galindo-Zaldivar et al., 2009; Medina, 1995; Meghraoui et al., 1996; Thauvin, 1971). The bay is bounded to the west by a system of normal faults allowing the uplift of the Al Hoceima region as shown by the marine terraces west of the city. How NS-trending-normal faults are generated in a general compressional setting NW-SE remains an open question, but it may be explained by the fact that either they are inherited faults from the Rif cordillera build-up during the NS Eurasian and African plates

convergence (Lonergan and White, 1997), or/and they are neo-formed faults related to the NE-SW transtensional motion in the northeastern Rif as evidenced by structural geology and geodetic studies (Chalouan et al., 2006; Vernant et al., 2010). In addition, the horst/graben succession observed in the Al-Hoceima region might have been triggered by the accommodation of the regional uplift of the northeastern Rif.

South of the Al Hoceima bay, the Trougout fault connects to the Bou Haddad fault, which shows mainly a normal component, and, further south, the Bou Haddad fault connects to the Nekor fault. Although previous studies suggest that the Nekor fault is inactive (Galindo-Zaldivar et al., 2009; Hatzfeld et al., 1993), there are some clear evidences of a left-lateral motion modifying the drainage network of the Jebel Izra and the drainage network between the oued Tarzout and oued Sidi Aisa at the northeast of the Jebel Izra. How the Nekor fault behaves at its western extremity (is it connecting to the southern Rif?), remains an open question, but evidences of activity along the southern front of the Rif in the region of Fez shows that the present day deformation extends there, consistently with the instrumental and historical seismicity (Moratti et al., 2003). This suggest a continuum with the N-S to NW-SE oriented Neogene compression (Bargach et al., 2004; Charroud et al., 2007) (Fig. 20).

## 6. Conclusion

All these observations are consistent with the kinematics that can be deduced from the GPS velocity field (Koulali et al., 2011; Vernant et al., 2010; Pérouse et al., 2010). Indeed, along the Mediterranean Sea, differential motion between Africa and the Northern Rif highlighted by GPS is consistent with the vertical motion of this region. Moreover, no GPS displacements relative to stable Africa can be detected along the Atlantic shore of the Rif in agreement with the lack of vertical motion (Meghraoui et al.,

1996; Morel and Meghraoui, 1996). However the rate deduced for the Trougout fault is lower than the one based on the GPS measurements. This is probably due to the fact that (i) the moderate earthquakes (<M 6.5) do not break the surface has evidenced by the Al Hoceima earthquakes (Galindo-Zaldivar et al., 2009) and/or (ii) the movement is partitioned in several minor faults distributed over the Al-Hoceima area. These might be the case also for the Nekor fault where we have evidenced left-lateral displacements of the drainage network, but only for 20–40 m of finite displacement. This implies that defining the active fault zones in the Rif relies on a careful analysis of subtle geomorphic features, where the fault rupture is partly distributed before reaching the surface, and the erosion processes quickly remove the features associated to the surface ruptures.

## Acknowledgments

We thank J. Chéry, J.-J. Cornée, M. Ferry and P. Munch for fruitful discussions and C. Astoury for the pre-processing of the rock samples. This research was supported in part by the “Institut National des Sciences de l’Univers” (INSU-CT3) and the “Center National d’Etudes Spatiales” (CNES-TOSCA). We are grateful to the “Center National de la Recherche Scientifique et Technique”, Rabat, for providing a car and a driver for the field work.

## References

- Aït Brahim, L., Chotin, P., 1990. Oriental Moroccan Neogene volcanism and strike-slip faulting. *J. Afr. Earth Sci. (Middle East)* 11, 273–280.
- Aït Brahim, L., Chotin, P., Tadili, B., Ramdani, M., 1990. Failles actives dans le Rif central et oriental. *C. R. Acad. Sci. Paris* 310, 1123–1129.
- Anderson, R.S., Densmore, A.L., Ellis, M.A., 1999. The generation and degradation of marine terraces. *Basin Res.* 11, 7–19.
- Bargach, K., Ruano, P., Chabli, A., Galindo-Zaldivar, J., Chalouan, A., Jabaloy, A., Akil, M., Ahmamou, M., de Galdeano, C.S., Benmakhlof, M., 2004. Recent tectonic deformations and stresses in the frontal part of the Rif Cordillera and the Saiss basin (Fes and Rabat regions, Morocco). *Pure Appl. Geophys.* 161, 521–540.
- Bintanja, R., van de Wal, R.S.W., Oerlemans, J., 2005. Modelled atmospheric temperatures and global sea levels over the past million years. *Nature* 437, 125–128.
- Blard, P.H., Lave, J., Pik, R., Quidelleur, X., Bourles, D., Kieffer, G., 2005. Fossil cosmogenic He-3 record from K-Ar dated basaltic flows of Mount Etna volcano (Sicily, 38 degrees N): evaluation of a new paleoaltimeter. *Earth Planet. Sci. Lett.* 236, 613–631.
- Blard, P.-H., Lave, J., Sylvestre, F., Placzek, C.J., Claude, C., Galy, V., Condom, T., Tibari, B., 2013. Cosmogenic He-3 production rate in the high tropical Andes (3800 m, 20 degrees S): implications for the local last glacial maximum. *Earth Planet. Sci. Lett.* 377, 260–275.
- Bradley, W.C., Griggs, G.B., 1976. Form, genesis, and deformation of central California wave-cut platforms. *Geol. Soc. Am. Bull.* 87, 433–449.
- Buñorn, E., Udiás, A., Madariaga, R., 1991. Intermediate and deep earthquakes in Spain. *Pure Appl. Geophys.* 136, 375–393.
- Calvert, A., Gomez, F., Seber, D., Barazangi, M., Jabolour, N., Ibenbrahim, A., Demnati, A., 1997. An integrated geophysical investigation of recent seismicity in the Al-Hoceima region of north Morocco. *Bull. Seismol. Soc. Am.* 87, 637–651.
- Calvert, A., Sandvol, E., Seber, D., Barazangi, M., Roecker, S., Mourabit, T., Vidal, F., Alguacil, G., Jabolour, N., 2000. Geodynamic evolution of the lithosphere and upper mantle beneath the Alboran region of the western Mediterranean: constraints from travel time tomography. *J. Geophys. Res. Solid Earth* 105, 10871–10898.
- Chalouan, A., Galindo-Zaldivar, J., Akil, M., Marin, C., Chabli, A., Ruano, P., Bargach, K., De Galdeano, C.S., Benmakhlof, M., Ahmamou, M., Gourari, L., 2006. Tectonic wedge escape in the southwestern front of the Rif Cordillera (Morocco). In: Moratti, G., Chalouan, A. (Eds.), *Tectonics of the Western Mediterranean and North Africa*. Geological Society Publishing House, Bath, pp. 101–118.
- Chalouan, A., Michard, A., 2004. The Alpine Rif belt (Morocco): a case of mountain building in a subduction–subduction–transform fault triple junction. *Pure Appl. Geophys.* 161, 489–519.
- Chalouan, A., Michard, A., Feinberg, H., Montigny, R.A., Saddiqi, O., 2001. The Rif mountain building (Morocco): a new tectonic scenario. *Bull. Soc. Geol. Fr.* 172, 603–616.
- Chappell, J., Shackleton, N., 1986. Oxygen isotopes and sea-level. *Nature* 324, 137–140.
- Charroud, M., Cherai, B., Benabdellahi, M., Falgueres, C., 2007. Quaternary neotectonic impact on the Sais sedimentary dynamic (Morocco): from Pliocene basin fore-chain to quaternary continental shelf. *Quaternaire* 18, 327–334.
- Choubert, G., Faure-Muret, A., Hilali, E.A., Houzay, J.P., de Lamotte, D.F., 1984. Carte géologique du Rif au 1/50,000, feuille Boudinar. *Notes Mém. Serv. Géol. Maroc.* 299.
- Choukri A., HaKam O.-K. & Reyss J.-L. (2011).- Difficultés de datation des niveaux marins pléistocènes à l'aide de coquilles de mollusques fossiles : cas du niveau ouljien sur la côte du Haut Atlas au Maroc.- Carnets de Géologie / Notebooks on Geology, Brest, Article 2011/02 (CG2011\_A02).
- Choukri, A., Hakam, O.-K., Reyss, J.-L., Plaziat, J.-C., 2007. Radiochemical dates obtained by alpha spectrometry on fossil mollusk shell from the 5e Atlantic shoreline of the High Atlas, Morocco. *Appl. Radiat. Isotopes* 65, 883–890.
- El Alami, S.O., Tadili, B.A., Cherkaoui, T.E., Medina, F., Ramdani, M., Ibrahim, L.A., Harnafi, M., 1998. The Al Hoceima earthquake of May 26, 1994 and its aftershocks: a seismotectonic study. *Ann. Geofis.* 41, 519–537.
- El Azzouzi, M., Bernard-Griffiths, J., Bellon, H., Maury, R.C., Pique, A., Fourcade, S., Cotten, J., Hernandez, J., 1999. Evolution of the sources of Moroccan volcanism during the Neogene. *C. R. Acad. Sci. Ser. II A* 329, 95–102.
- El Bakkali, S., Gourgaud, A., Bourdier, J.-L., Bellon, H., Gundogdu, N., 1998. Post-collision neogene volcanism of the Eastern Rif (Morocco): magmatic evolution through time. *Lithos* 45, 523–543.
- El Kadiri, K., de Galdeano, C.S., Pedrera, A., Chalouan, A., Galindo-Zaldivar, J., Julià, R., Akil, M., Hlila, R., Ahmamou, M., 2010. Eustatic and tectonic controls on Quaternary Ras Leona marine terraces (Strait of Gibraltar, northern Morocco). *Quat. Res.* 74, 277–288.
- Faccenna, C., Piromallo, C., Crespo-Blanc, A., Jolivet, L., Rossetti, F., 2004. Lateral slab deformation and the origin of the western Mediterranean arcs. *Tectonics* 23.
- Fadil, A., Vernant, P., McClusky, S., Reilinger, R., Gomez, F., Ben Sari, D., Mourabit, T., Feigl, K., Barazangi, M., 2006. Active tectonics of the western Mediterranean: geodetic evidence for rollback of a delaminated subcontinental lithospheric slab beneath the Rif Mountains, Morocco. *Geology* 34, 529–532.
- Galindo-Zaldivar, J., Chalouan, A., Azzouz, O., Sanz de Galdeano, C., Anahnah, F., Ameza, L., Ruano, P., Pedrera, A., Ruiz-Constan, A., Marin-Lechado, C., Benmakhlof, M., Lopez-Garrido, A.C., Ahmamou, M., Saji, R., Roldan-Garcia, F.J., Akil, M., Chabli, A., 2009. Are the seismological and geological observations of the Al Hoceima (Morocco, Rif) 2004 earthquake (M=6.3) contradictory? *Tectonophysics* 475, 59–67.
- Hatzfeld, D., Caillot, V., Cherkaoui, T., Jebli, H., Medina, F., 1993. Microearthquake seismicity and fault plane solutions around the Nekor Strike-Slip-Fault, Morocco. *Earth Planet. Sci. Lett.* 120, 31–41.
- Kaufman, A., Broecker, W.S., Ku, T.-L., Thurber, D.L., 1971. The status of U-series methods of mollusk dating. *Geochim. Cosmochim. Acta* 35, 1155–1183.
- Kornprobst, J., 1974. Contributions à l'étude pétrographique et structurale de la zone interne du Rif (Maroc septentrional). *Notes Mém. Serv. géol. Maroc.* 251, 256 pp.
- Koulali, A., Ouazar, D., Tahayat, A., King, R.W., Vernant, P., Reilinger, R.E., McClusky, S., Mourabit, T., Davila, J.M., Amraoui, N., 2011. New GPS constraints on active deformation along the Africa–Iberia plate boundary. *Earth Planet. Sci. Lett.* 308, 211–217.
- Kurz, M., 1986. In situ production of terrestrial cosmogenic helium and some applications. *Geochim. Cosmochim. Acta* 50, 2855–2862.
- Leblanc, D., Olivier, P., 1984. Role of strike-slip faults in the Betic-Rifian orogeny. *Tectonophysics* 101, 345–355.
- Lonergan, L., White, N., 1997. Origin of the Betic-Rif mountain belt. *Tectonics* 16, 504–522.
- Ludwig, K.R., 2003. Mathematical-statistical treatment of data and errors for <sup>230</sup>Th/U geochronology. *Rev. Mineral. Geochim.* 52, 631–656.
- Ludwig, K.R., 2012. Using Isoplot/Ex, version 3.76, A Geochronological Toolkit for Microsoft Excel. Berkeley Geochronology Center Spec. Pub., pp. 6.
- Maldonado, A., Comas, M., 1992. Geology and geophysics of the Alboran Sea: an introduction. *Geo-Mar. Lett.* 12, 61–65.
- McClusky, S., Reilinger, R., Mahmoud, S., Ben Sari, D., Tealeb, A., 2003. GPS constraints on Africa (Nubia) and Arabia plate motions. *Geophys. J. Int.* 155, 126–138.
- Medina, F., 1995. Present-day state of stress in northern Morocco from focal mechanism analysis. *J. Struct. Geol.* 17, 1035–1046.
- Medina, F., El Alami, S.O., 2006. Focal mechanisms and state of stress in the Al Hoceima area (Central Rif, Morocco). *Bull. Inst. Sci. Rabat, Sect. Sci. Terre.* 28, 19–30.
- Meghraoui, M., 1991. Blind Reverse Faulting System Associated with the Mont Chenoua-Tipaza Earthquake of 29 October 1989 (north-Central Algeria). *Terra Nova* 3, 84–93.
- Meghraoui, M., Morel, J.-L., Andrieux, J., Dahmani, M., 1996. Pliocene and quaternary tectonics of the Tell-Rif mountains and Alboran sea, a complex zone of continent convergence. *Bull. Soc. Geol. Fr.* 167, 141–157.
- Moratti, G., Piccardi, L., Vannucci, G., Belardinelli, M.E., Dahmani, M., Bendkik, A., Chenakeb, M., 2003. The 1755 “Meknes” earthquake (Morocco): field data and geodynamic implications. *J. Geodyn.* 36, 305–322.
- Morel, J.-L., 1987. Evolution récente de l'orogène rifain et de son avant-pays depuis la fin de la mise en place des nappes (Rif, Maroc).
- Morel, J.-L., Meghraoui, M., 1996. Goringe-Alboran-Tell tectonic zone: a transpression system along the Africa-Eurasia plate boundary. *Geology* 24, 755–758.
- Palumbo, L., Benedetti, L., Bourles, D., Cinque, A., Finkel, R., 2004. Slip history of the Magnola fault (Apennines, Central Italy) from Cl-36 surface exposure dating: evidence for strong earthquakes over the Holocene. *Earth Planet. Sci. Lett.* 225, 163–176.
- Pelaez, J.A., Chourak, M., Tadili, B.A., Brahim, L.A., Hamdache, M., Lopez Casado, C., Martinez Solares, J.M., 2007. A catalog of main Moroccan earthquakes from 1045 to 2005. *Seismol. Res. Lett.* 78, 614–621.
- Pérouse, E., Vernant, P., Chéry, J., Reilinger, R., McClusky, S., 2010. Active surface deformation and sub-lithospheric processes in the Western Mediterranean constrained by numerical models. *Geology* 38, 823–826, <http://dx.doi.org/10.1130/g30963.1>.

- Plaziat, J.-C., Aberkan, M., Ahmamou, M., Choukri, A., 2008. The quaternary deposits of Morocco. In: Michard, A., Saddiqi, O., Chalouan, A., Lamotte, D.F.de (Eds.), *Continental Evolution: The Geology of Morocco*, Lecture Notes in Earth Sciences. Springer, Berlin/Heidelberg, pp. 359–376.
- Rampnoux, J.-P., Angelier, J., Colleta, B., Fudral, S., Guillemin, M., Pierre, G., 1977. L'histoire tectonique récente (Tortonien à Quaternaire) de l'Arc de Gibraltar et des bordures de la mer d'Alboran. Les résultats de l'analyse structurale et de la néotectonique des littoraux. B: Les résultats de l'analyse structurale au Maroc. *Bull. Soc. géol. Fr.* 7, 193, 594–599.
- Scarsi, P., 2000. Fractional extraction of helium by crushing of olivine and clinopyroxene phenocrysts: effects on the He-3/He-4 measured ratio. *Geochim. Cosmochim. Acta* 64, 3751–3762.
- Stearns, C.E., Thurber, D.L., 1965. Th<sup>230</sup>/U<sup>234</sup> dates of late Pleistocene marine fossils from the Mediterranean and Moroccan littorals. *Progr. Oceanogr.* 4, 293–305.
- Stich, D., Mancilla, F.D., Baumont, D., Morales, J., 2005. Source analysis of the M-w 6.3 2004 Al Hoceima earthquake (Morocco) using regional apparent source time functions. *J. Geophys. Res. Solid Earth*, 110.
- Stone, J.O., 2000. Air pressure and cosmogenic isotope production. *J. Geophys. Res. Solid Earth* 105, 23753–23759.
- Tahayt, A., Feigl, K.L., Mourabit, T., Rigo, A., Reilinger, R., McClusky, S., Fadil, A., Berthier, E., Dorbath, L., Serroukh, M., Gomez, F., Ben Sari, D., 2009. The Al Hoceima (Morocco) earthquake of 24 February 2004, analysis and interpretation of data from ENVISAT ASAR and SPOT5 validated by ground-based observations. *Remote Sens. Environ.* 113, 306–316.
- Talvitie, N.A., 1972. Electrodeposition of actinides for alpha spectrometric determination. *Anal. Chem.* 44, 280–283.
- Thauvin, J.P., 1971. Ressources en eau du Maroc, domaine du Rif et du Maroc oriental. *Notes Mém. Serv. Géol. Maroc.*, 231.
- Trull, T., Kurz, M., 1993. Experimental measurements of He-3 and He-4 mobility in olivine and clinopyroxene at magmatic temperatures. *Geochim. Cosmochim. Acta* 57, 1313–1324.
- Trull, T.W., Kurz, M.D., Jenkins, W.J., 1991. Diffusion of cosmogenic <sup>3</sup>He in olivine and quartz: implications for surface exposure dating. *Earth Planet. Sci. Lett.* 103, 241–256.
- Vernant, P., Fadil, A., Mourabit, T., Ouazar, D., Koulaï, A., Martin Davila, J., Garate, J., McClusky, S., Reilinger, R., 2010. Geodetic constraints on active tectonics of the Western Mediterranean: implications for the kinematics and dynamics of the Nubia-Eurasia plate boundary zone. *J. Geodyn.* 49, 123–129.
- Wells, D.L., Coppersmith, K.J., 1994. New empirical relationships among magnitude, rupture length, rupture width, rupture area, and surface displacement. *Bull. Seismol. Soc. Am.* 84, 974–1002.
- Wildi, W., 1983. The orogenic belt of the Rif (morocco) and the Tell (algeria, Tunisia) – structure, stratigraphy, paleogeographic and tectonic evolution from Triassic to the Miocene. *Rev. Geol. Dyn. Geogr. Phys.* 24, 201–297.
- Zazo, C., Goy, J., Dabrio, C., Bardaji, T., Somoza, L., Silva, P., 1993. The last interglacial in the Mediterranean as a model for the present interglacial. *Glob. Planet. Change* 7, 109–117.
- Zazo, C., Silva, P.G., Goy, J.L., Hillaire-Marcel, C., Ghaleb, B., Lario, J., Bardaji, T., González, A., 1999. Coastal uplift in continental collision plate boundaries: data from the last interglacial marine terraces of the Gibraltar Strait area (south Spain). *Tectonophysics* 301, 95–109.
- Zimmermann, L., Blard, P.H., Burnard, P., Medynski, S., Pik, R., Puchol, N., 2012. A new single vacuum furnace design for cosmogenic <sup>3</sup>He dating. *Geostand. Geoanal. Res.* 36, 121–129.